

# A Viscoelastic-Viscoplastic Model of Titanium Structures Subjected to Thermo-Chemo-Mechanical Environment

Hao Yan and Caglar Oskay\*

Department of Civil and Environmental Engineering  
Vanderbilt University  
Nashville, TN 37235

## Abstract

This manuscript provides a new viscoelastic-viscoplastic deformation model for oxygen-assisted embrittlement and degradation of titanium structures subjected to combined loading and environments. The viscoelastic-viscoplastic formulation accounts for the creep/relaxation behavior at elevated temperatures within the coupled processes of oxygen transport and deformation. The viscoelastic behavior is modeled based on the Boltzmann integral and Prony series approximation of the time-dependent moduli. The concentration-dependent viscoplastic deformation response is idealized using a generalized Johnson-Cook plasticity model. The proposed deformation model is fully coupled with a transport model to describe the ingress of oxygen into the structure. The coupled transport-deformation model is implemented using a three-field formulation, in which concentration, displacement and pressure are evaluated as independent unknowns. The computational model was validated against experiments conducted in combined environments on the high temperature alloy Ti-6242S. A detailed investigation of the coupling mechanisms between the oxygen ingress induced embrittlement, relaxation and the inelastic deformation is provided, including partial validation of the interaction mechanisms based on experimental data.

*Keywords:* Multiphysics; Coupled problems; Environmental effects; Viscoelastic-Viscoplastic; Oxygen embrittlement.

## 1 Introduction

Understanding and predicting the mechanical performance of metallic material and structural systems operating in combined environments have been active research topics for

---

\*Corresponding author address: VU Station B#351831, 2301 Vanderbilt Place, Nashville, TN 37235. Email: caglar.oskay@vanderbilt.edu

decades. Combined environment refers to the simultaneous presence of potentially aggressive environmental agents, elevated temperatures and thermal loads, and a variety of mechanical loads. In a combined high-temperature environment, aggressive environmental elements tend to deteriorate the mechanical performance of the material. A case in point is the effect of oxygen ingress into titanium alloys, which results in significant changes in the material properties including embrittlement, increased hardness, and dramatic reduction in fatigue life [6, 16].

Modeling and prediction of the oxygen ingress induced deterioration in structures made of titanium and other alloys is of particular concern for aerospace structural components employed in hypersonic air vehicles. The perceived operating thermo-mechanical conditions for hypersonic structures are typically at the upper end of the capability spectra of titanium alloys. In the presence of high temperatures, atmospheric oxygen tends to diffuse into the alloy, leading to the deterioration of the material properties marked by a strong coupling between oxygen transport and mechanical deformation. The presence of elevated concentrations of oxygen at lattice interstitials and trap sites (e.g., dislocations) causes lattice straining, and inhibits dislocation glide, leading to hardening and embrittlement (i.e., early onset of fracture initiation). Further increase of oxygen content leads to phase transformation (e.g., from  $\beta$  to  $\alpha$ ) and formation of an oxide layer. The diffusion of oxygen is also affected by the deformation processes and damage state since the microcrack formation within the brittle oxygen-rich layer as dislocations serve as preferential sites for oxygen. The presence of surface microcracks and microvoids that typically (but not necessarily) originate at the triple junctions and at grain boundaries also enhances diffusivity of oxygen deeper towards the interior of the structure.

Extensive research exists on experimental and modeling based investigations of oxygen ingress into titanium alloys (e.g., [3, 5, 12, 32]). A comprehensive review of earlier diffusivity characterization of titanium and titanium alloys is provided by Liu and Welsch [19]. In contrast, investigations of the coupling mechanisms between oxygen transport, deformation and damage have been relatively scarce. Peters et al. [27] experimentally investigated the effect of mechanical loading on the oxygen transport rates. Applied loading beyond yielding showed nominal acceleration of oxygen ingress at elevated temperatures. The authors pointed to the effect of very significant relaxation that dominates the response under sustained deformations, which complicates the coupling between the transport and mechanical processes. Parthasarathy et al. [26] proposed a fatigue life prediction methodology for oxygen exposed Titanium alloys subjected to uniaxial tension loads. Pilchak et al. [28] provided experimental and fractographic investigation of the effect of high temperature exposure of a near- $\alpha$  titanium alloy undergoing oxygen ingress. More recently Refs. [25, 36] developed a computational transport-deformation model that accounts for the coupling mechanisms between the

two physical processes. This model does not adequately account for the relaxation processes that significantly affect both the mechanical response and the coupling mechanisms.

In this manuscript, a new coupled deformation-transport model is proposed to study the response of titanium alloys at combined environments. The proposed approach builds on the model by Ref. [25] by extending it to account for creep and relaxation processes, which are critical to the response characterization at high temperatures. The coupled-transport model is implemented using a three field formulation, in which concentration, displacement and pressure are evaluated as independent unknowns [36]. The transport solver includes pressure dependent advection and reaction terms, which are stabilized using the Galerkin least-squares stabilization method [9]. The computational model was validated against experiments conducted in combined environments. The two main novel contributions of this manuscript are: (1) The proposed model accurately captures the time-dependent creep/relaxation processes through the incorporation of viscoelastic-viscoplastic mechanisms. The authors' previous modeling work did not provide the necessary relaxation mechanisms at elevated temperatures [25]; (2) A detailed investigation of the coupling mechanisms between the oxygen ingress induced embrittlement, relaxation and the inelastic deformation is provided, including partial validation of the interaction mechanisms based on experimental data.

The remainder of this manuscript is organized as follows: Section 2 provides the formulation of viscoelastic-viscoplastic model coupled with the oxygen transport model. The finite element implementation of the viscoelastic-viscoplastic deformation model is described in Section 3. Section 4 details the numerical investigation of a high-temperature titanium alloy of interest, Ti-6242S, subjected to combined loading and high temperature environment. The calibration of the proposed model based on the independent set of experimental data and a detailed analysis of the failure and relaxation characteristics of oxygen-exposed specimens are included in this section. The conclusions and future research directions are included in Section 5.

## 2 Problem Statement

The problem domain is described in Fig. 1, where the solid body,  $\Omega \subset \mathbb{R}^{n_{sd}}$  is subjected to an aggressive agent (oxygen) at the exterior surfaces of the problem domain ( $n_{sd}$ : number of space dimensions). The ingressed oxygen results in a more brittle and hardening material compared to the substrate alloy, where surface cracks will initiate under mechanical loading, as shown in Fig. 1. In this section the viscoelastic-viscoplastic deformation model is formulated together with the transport model. The oxidation mechanism as well as its effects on mechanical property degradation including the loss of ductility and hardening are investigated.

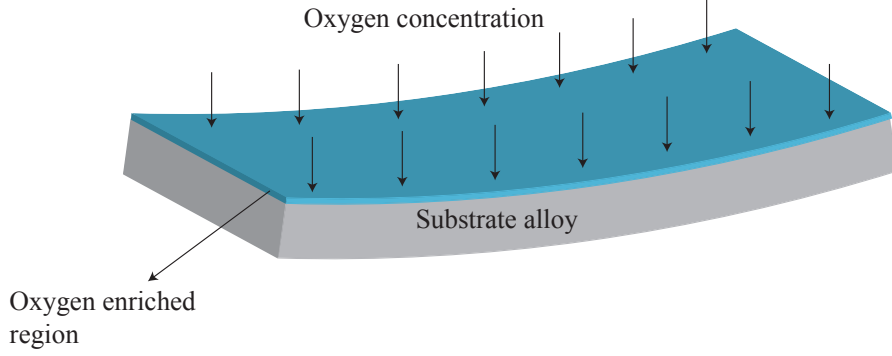


Figure 1: Structural component subjected to coupled transport-deformation processes.

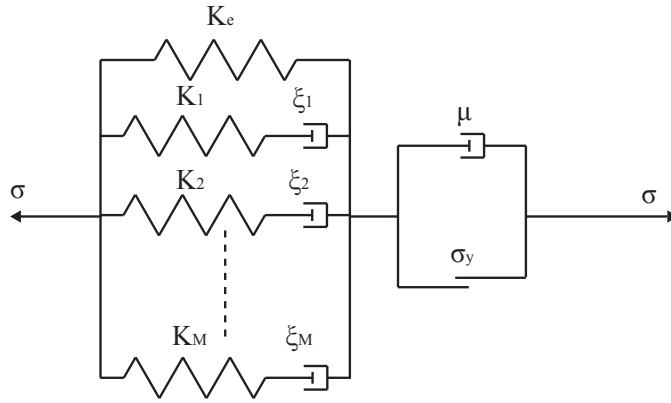


Figure 2: One dimensional rheological representation of the viscoelastic-viscoplastic model.

## 2.1 Deformation Model

In this section, a viscoelastic-viscoplastic model is defined to describe deformation behavior in the presence of aggressive agents that affect the mechanical response. The model presented here extends the coupled transport-deformation model presented in [25] to account for the relaxation/creep behavior, which is predominant in combined environment response at elevated temperatures, which also activates aggressive agent transport within the solid. In particular, the alloys of interest could demonstrate relaxation up to near stress-free states at elevated temperatures (see Section 4). The purpose of the proposed model is to accurately idealize the short-term (i.e., a few seconds) and the long-term (i.e., in the order of hours) time dependent creep/relaxation behavior. From the rheological perspective, the viscoelastic-viscoplastic model is a three-dimensional generalization of Wiechert springs serially connected to a viscoplastic device as illustrated in Fig. 2.

The governing equilibrium equations describing the mechanical response is expressed in the following form:

$$s_{ij,j}(\mathbf{x}, t) - p_{,i}(\mathbf{x}, t) + b_i(\mathbf{x}, t) = 0 \quad (1)$$

where,  $\mathbf{b}$  the body force per unit volume;  $\mathbf{s}$  is the deviatoric stress tensor;  $p = -\text{tr}(\boldsymbol{\sigma})/3$  the pressure;  $\boldsymbol{\sigma}$  the stress tensor ( $\boldsymbol{\sigma} = \mathbf{s} - p\boldsymbol{\delta}$ );  $\boldsymbol{\delta}$  the second order identity tensor; and  $\text{tr}(\cdot)$  denotes trace. We adopt the index notation in the problem formulation (i.e.,  $i = 1, \dots, n_{\text{sd}}$ ). Repeated indices of the spatial dimensions indicate summation unless otherwise stated. A subscript followed by a comma indicates partial derivative (i.e.,  $f_{,i} = \partial f / \partial x_i$ ).  $\mathbf{x}$  and  $t$  parameterize the spatial and temporal dimensions, respectively. Bold symbol indicates vector notation (i.e.,  $\mathbf{x} = [x_1, x_2, x_3]$  for  $n_{\text{sd}} = 3$ ) and superscribed dot indicates differentiation with respect to time. The following boundary conditions are prescribed to evaluate the mechanical problem:

$$u_i(\mathbf{x}, t) = \bar{u}_i(\mathbf{x}, t) \quad \mathbf{x} \in \Gamma_D^u \quad (2)$$

$$\sigma_{ij}n_j = \bar{t}_i(\mathbf{x}, t) \quad \mathbf{x} \in \Gamma_N^u \quad (3)$$

where,  $\mathbf{u}$  denotes the displacement vector field;  $\bar{\mathbf{u}}$  is the prescribed displacement along the Dirichlet boundary;  $\Gamma_D^u$ ;  $\bar{\mathbf{t}}$  the prescribed traction along the Neumann boundary,  $\Gamma_N^u$ , such that  $\Gamma_D^u \cap \Gamma_N^u = \emptyset$  and  $\Gamma_D^u \cup \Gamma_N^u = \Gamma$ ; and  $\mathbf{n}$  the outer unit normal to the traction boundary.

Assuming small strain kinematics, the total strain tensor,  $\boldsymbol{\varepsilon}$ , is:

$$\varepsilon_{ij} = \frac{1}{2} (u_{i,j}(\mathbf{x}, t) + u_{j,i}(\mathbf{x}, t)) \quad (4)$$

The adoption of the small strain theory implies that large rotations and large plastic deformations that may be present in some high temperature applications are not included in this study. The total deformation in the viscoelastic-viscoplastic model is separated into four components:

$$\varepsilon_{ij} = \varepsilon_{ij}^{\text{ve}} + \varepsilon_{ij}^{\text{vp}} + \varepsilon_{ij}^{\text{T}} + \varepsilon_{ij}^{\text{c}} \quad (5)$$

$\boldsymbol{\varepsilon}^{\text{ve}}$ ,  $\boldsymbol{\varepsilon}^{\text{vp}}$ ,  $\boldsymbol{\varepsilon}^{\text{T}}$  and  $\boldsymbol{\varepsilon}^{\text{c}}$  respectively denote the viscoelastic, viscoplastic, thermal and elevated aggressive agent concentration induced strain, respectively.

The constitutive relationship between the deviatoric stress and the viscoelastic strain is modeled using the Boltzmann superposition integral in the context of linear viscoelasticity:

$$s_{ij}(t) = \int_0^t L'_{ijkl}(t - \tau) \frac{d\varepsilon_{kl}^{\text{ve}}(\tau)}{d\tau} d\tau \quad (6)$$

in which, the spatial dependence of the pertinent fields is suppressed for simplicity.  $\mathbf{L}'$  is the time-dependent deviatoric component of the tensor of viscoelastic moduli, taken to be

symmetric and positive definite at any time during the deformation process:

$$L'_{ijkl} = L'_{klij} = L'_{jikl} = L'_{ijlk} \quad (7)$$

$$\zeta_{ij} L'_{ijkl} \zeta_{kl} \geq \eta \zeta_{ij} \zeta_{ij}; \quad \forall \zeta_{ij} = \zeta_{ji}; \quad \eta > 0 \quad (8)$$

A convenient time evolution expression for the viscoelastic moduli is the Prony series:

$$L'_{ijkl}(t) = \left[ K_e + \sum_{m=1}^M K_m \exp\left(-\frac{t}{\xi_m}\right) \right] \bar{L}'_{ijkl} \quad (9)$$

in which,  $\bar{\mathbf{L}}'$  is a time independent moduli tensor;  $M$  the number of Maxwell elements incorporated in the Wiechert model;  $K_e$  is the ratio of equilibrium deviatoric moduli over instantaneous deviatoric moduli; and  $K_m$  and  $\xi_m$  are the ratio of deviatoric moduli on  $m^{\text{th}}$  Maxwell element over instantaneous deviatoric moduli and the time parameters in the  $m^{\text{th}}$  Maxwell element, respectively. By employing the above expression, all components of the viscoelastic moduli relax uniformly. A straightforward generalization to component-dependent relaxation is possible by using a slightly modified version of the Prony series approximation. By constraining the values of the Prony series parameters such that  $K_e + \sum_{m=1}^M K_m = 1$ , the time independent moduli tensor becomes the instantaneous elastic moduli; i.e.,  $\bar{\mathbf{L}}' = \mathbf{L}'(t=0)$ .

For an isotropic solid, the deviatoric component of the elastic moduli is expressed as:

$$L'_{ijkl}(t) = 2G(t) \left( \delta_{ik}\delta_{jl} - \frac{1}{3}\delta_{ij}\delta_{kl} \right) \quad (10)$$

Substituting Eqs. 9 and 10 into Eq. 6, the deviatoric stress tensor is expressed as:

$$s_{ij}(t) = 2\bar{G}K_e\varepsilon_{ij}^{\text{ve}}(t) + 2\bar{G}\sum_{m=1}^M K_m\varepsilon_{ij}^m(t) \quad (11)$$

where,

$$\varepsilon_{ij}^m(t) = \int_0^t \exp\left(-\frac{t-\tau}{\xi_m}\right) \frac{d\varepsilon_{ij}^{\text{ve}}(\tau)}{d\tau} d\tau \quad (12)$$

in which,  $\varepsilon^{\text{ve}}$  is the deviatoric component of the viscoelastic strain, and  $\bar{G} = G(0)$  the instantaneous shear modulus.

The variation of the relaxation behavior as a function of temperature is modeled using the Williams-Landel-Ferry (WLF) equation. Let  $a_T$  denote the WLF time-temperature shift factor expressed in the form:

$$\log a_T(T) = \frac{-C_1(T - T_{\text{ref}})}{C_2 + (T - T_{\text{ref}})} \quad (13)$$

where,  $T$  denotes temperature;  $C_1$  and  $C_2$  are material constants and  $T_{\text{ref}}$  is the reference temperature, taken to be the room temperature in this study. Provided the relaxation behavior at the reference temperature and the material constants are known, the relaxation behavior at an arbitrary temperature is obtained by shifting the time scale within a master WLF curve using  $a_T$ :

$$t = \int_0^\tau \frac{d\xi}{a_T(T(\xi))} \quad (14)$$

The thermal and aggressive agent concentration induced strains are taken to be volumetric:

$$\varepsilon_{ij}^T = \alpha (T - T_{\text{ref}}) \delta_{ij} \quad (15)$$

$$\varepsilon_{ij}^c = \vartheta (c - c_\infty) \delta_{ij} \quad (16)$$

where,  $\alpha$  is the thermal expansion coefficient;  $c$  the concentration; and  $\vartheta$  the concentration induced volumetric expansion coefficient. The viscoplastic strain is taken to remain in the deviatoric strain space (i.e.,  $\text{tr}(\boldsymbol{\varepsilon}^{\text{vp}}) = 0$ ). Considering an isotropic solid with insignificant relaxation under hydrostatic loading, the constitutive relationship for pressure becomes:

$$p(t) = -ku_{i,i}(t) + 3k [\alpha (T(t) - T_0) + \vartheta (c(t) - c_\infty)] \quad (17)$$

in which,  $k$  is the bulk modulus.

The evolution of the viscoplastic strain is modeled by a generalization of the Johnson-Cook plasticity model to account for the effects of elevated aggressive agent concentration. The viscoplastic model employed in this study accounts for the effects of embrittlement and hardening as a function of the aggressive agent concentration [25]. The flow rule of the viscoplastic strain is expressed in terms of a power law:

$$\dot{\varepsilon}_{ij}^{\text{vp}} = \gamma \left\langle \frac{f}{\sigma_Y} \right\rangle^{q(T^*)} \frac{\partial f}{\partial \sigma_{ij}} \quad (18)$$

where,  $\gamma$  is the fluidity parameter;  $\langle \cdot \rangle$  denotes Macaulay brackets (i.e.,  $\langle \cdot \rangle = ((\cdot) + |\cdot|)/2$ );  $\sigma_Y$  the flow stress; and  $f(\boldsymbol{\sigma}, \sigma_Y)$  the loading function. The viscoplastic hardening exponent,  $q$ , is expressed as a function of the non-dimensional temperature,  $T^*$ , as:

$$q(T^*) = q_{\text{ref}} + (\bar{q} - q_{\text{ref}})T^*; \quad T^* = \frac{T - T_{\text{ref}}}{T - T_{\text{ref}}} \quad (19)$$

where  $q_{\text{ref}} = q(T_{\text{ref}})$  and  $\bar{q} = q(\bar{T})$  are exponents evaluated at two temperatures.

The Von-Mises loading function is adopted in this study:

$$f(\sigma_{ij}, \sigma_Y) = \sigma_{eq} - \sigma_Y = \sqrt{3\bar{s}} - \sigma_Y \quad (20)$$

in which,  $\sigma_{eq}$  is the equivalent stress; and  $\bar{s}$  the second invariant of the deviatoric stress,  $\mathbf{s}$ . The generalized Johnson-Cook flow stress provides a functional relationship between yielding and the strain, temperature and concentration:

$$\sigma_Y = [A + B(\bar{\varepsilon}^{vp})^n + F(c - c_\infty)][1 - (T^*)^m] \quad (21)$$

in which  $A, B, F, m$  and  $n$  are material parameters. When the non-dimensional temperature reaches unity, Eq. 21 implies complete lack of material strength. In some applications of similar models, the non-dimensional temperature is expressed using the melting temperature (i.e.,  $\bar{T} = T_{\text{melt}}$ ). For the titanium alloys of interest, the extrapolation of the experimental data on the yield strength variation as a function of temperature indicates vanishing yield strength at around the beta transus temperature. We therefore use  $\bar{T} = T_\beta$  in this study. It must be noted that it is impractical to characterize  $q$  in Eq. 19 by an experiment conducted at the beta transus temperature. Since the temperature variation of the exponent is linear, an experiment conducted at any temperature between  $T_{\text{ref}}$  and  $T_\beta$  is sufficient to identically calibrate  $q$ .

The equivalent viscoplastic strain  $\bar{\varepsilon}^{vp}$  is defined as:

$$\bar{\varepsilon}^{vp} = \sqrt{\frac{2}{3} \varepsilon_{ij}^{vp} : \varepsilon_{ij}^{vp}} \quad (22)$$

The damage progression within the material is modeled as a function of temperature and concentration. Let the damage parameter,  $\omega$ , be the ratio between the equivalent strain,  $\bar{\varepsilon}^{vp}$  and the failure strain,  $\varepsilon_f$ :

$$\omega = \frac{\bar{\varepsilon}^{vp}}{\varepsilon_f} \quad (23)$$

$\omega \in [0, 1)$  denotes the state of damage at a material point, with  $\omega=0$  indicating no additional defect compared to the initial state, and,  $\omega=1$  corresponds to loss of load carrying capacity at the material point. The failure strain  $\varepsilon_f$  is described as:

$$\varepsilon_f = D_1(c) (1 + D_5 \exp(D_6 T^*)) \quad (24)$$

in which,  $D_5$  and  $D_6$  parameterizes the effect of temperature on the failure strain.  $D_1$  varies as a function of concentration and idealizes the progressive embrittlement due to aggressive

agent ingress:

$$D_1(c) = \begin{cases} D_1^\infty & \text{if } c \leq c_\infty \\ \frac{1}{c_\infty - c_{\text{crit}}} ((D_1^\infty - D_1^\alpha) c + D_1^\alpha c_\infty - D_1^\infty c_{\text{crit}}) & \text{if } c_\infty < c < c_{\text{crit}} \\ D_1^\alpha & \text{if } c \geq c_{\text{crit}} \end{cases} \quad (25)$$

$D_1^\infty$  denotes the failure strain at room temperature in the absence of elevated concentration;  $D_1^\alpha$  denotes failure strain beyond a critical concentration,  $c_{\text{crit}}$ ; and the embrittlement is assumed to be linear at intermediate concentration values. The effect of aggressive agent ingress on the mechanical response is modeled based on the concentration dependent terms in Eqs. 21 and 25. In Eq. 21, the flow stress is affected by the concentration. Elevated concentration tends to harden the material. In addition to hardening, the elevated concentration embrittles the response by reducing the failure strain in Eq. 24.

In an alternative approach, the plasticity theory has been extended to account for relaxation below the yield values and employed to describe cyclic response at high temperature [4]. This approach presents a model that can also capture the viscoelastic response in cyclic loading through viscoplastic modeling together with pure kinematic hardening. The key assumption made is the vanishing threshold for yielding, which links the response to the viscoelastic regime. The treatment of viscoelasticity is spectral in contrast to the integral type viscoelasticity considered herein. The approach taken in this manuscript therefore constitutes a complimentary proposition to the ideas of Ref. [4].

## 2.2 Transport Model

By incorporating Oriani's equilibrium theory to describe the diffusion of the aggressive agent into the stressed solid [18] and considering the effect of stress on the diffusion process, the governing equation of the aggressive agent transport is expressed as an advection-reaction-diffusion problem of the form:

$$\dot{c} - (Dc_{,i})_{,i} + \alpha_i c_{,i} + \beta c = 0 \quad (26)$$

in which,  $D$  is the diffusivity of the aggressive agent within the solid, and  $c$  the concentration of aggressive agent, given as weight ratio of the diffusing agent and the solid substrate within an infinitesimal control volume.  $\alpha_i$  and  $\beta$  are coefficients of advection and reaction, respectively, expressed as a function of pressure gradient and Laplacian:

$$\alpha_i = -\frac{D\bar{V}_c}{RT} p_{,i} \quad (27)$$

$$\beta = \left( \frac{D\bar{V}_c T_{,i}}{RT^2} - \frac{D_{,i}\bar{V}_c}{RT} \right) p_{,i} - \frac{D\bar{V}_c}{RT} p_{,ii} \quad (28)$$

in which,  $R$  is the universal gas constant; and  $\bar{V}_c$  the partial molar volume of the ingressed gas in the substrate solid.

The initial and boundary conditions for the transport problem are expressed as:

$$c(\mathbf{x}, t = 0) = c_\infty(\mathbf{x}); \quad \mathbf{x} \in \Omega \quad (29)$$

$$c(\mathbf{x}, t) = c_0(\mathbf{x}, t); \quad \mathbf{x} \in \Gamma_c \quad (30)$$

$$q_i(\mathbf{x}, t) n_i = 0; \quad \mathbf{x} \in \Gamma_q \quad (31)$$

in which,  $c_\infty$  is the concentration of the aggressive agent at the natural state of the solid;  $c_0$  the boundary concentration prescribed along  $\Gamma_c$ ;  $\mathbf{q}$  the concentration flux; and  $\mathbf{n}$  the outward normal unit vector to the boundary,  $\Gamma_q$ .

The transport process is coupled to the mechanical deformation through two mechanisms. The first is the stress dependent advection and reaction flow, as shown in Eqs. 27 and 28. The second is by linking the diffusivity to the state of damage within the solid. Considering the enhancement of diffusivity as the increased defect density [30, 29, 14], the diffusivity is modeled based on the percolation theory [25] as:

$$D(\omega, T) = D_0 (1 + \mathcal{D}(\omega)) \exp\left(-\frac{Q}{RT}\right) \quad (32)$$

where,  $D_0$  is the pre-exponential constant;  $Q$  the activation energy; and,  $\mathcal{D}(\omega)$  the effect of mechanical damage on diffusivity:

$$\mathcal{D}(\omega) = \begin{cases} a\omega; & \omega < \omega_c \\ a\omega - \frac{(\omega - \omega_c)^2}{\omega - \omega_{ec}}; & \omega_c \leq \omega < \omega_{ec} \\ \infty; & \omega \geq \omega_{ec} \end{cases} \quad (33)$$

in which,  $\omega_c$  and  $\omega_{ec}$  denote the conduction and elastic percolation thresholds respectively; and,  $a$  is a material parameter.

The diffusivity is in a linear relationship with the damage variable when damage is smaller than the conduction percolation threshold value ( $\omega < \omega_c$ ) [30]. The state when the damage exceeds the elastic percolation threshold,  $\omega_{ec}$ , indicates a physical crack which allows free flow of the aggressive agent. Beyond  $\omega_{ec}$ ,  $\mathcal{D}(\omega)$  is assigned a large but finite value to avoid numerical instability. At intermediate values of the damage state, the diffusivity progressively increases as a function of damage [13].

The mechanical state in the proposed model influences transport in two ways: (1) the

increased diffusivity as a function of the damage parameter through damage percolation idea [14]; and (2) the advection induced by pressure gradients. In the presence of a distinct crack or notch (either initially present or formed during the process), the pressure gradients within the process zones produce a non-zero advection term in the transport equation and induce transport of the aggressive agent, even in the absence of elevated concentration around external boundaries. This capability of the model was demonstrated in Yan and Oskay [36]. Mechanism (1), in the absence of the formation of a distinct crack, does not introduce transport as only the apparent diffusivity parameter is increased by the presence of damage. In the investigations discussed in this manuscript (i.e., oxygen transport in a titanium alloy) the gradient-induced transport alone would not cause significant embrittlement since, the amount of oxygen content in the bulk alloy is very low (i.e., approximately 0.15 %wt).

### 3 Numerical Implementation of the Deformation Model

The deformation and transport models described in Section 2 are numerically evaluated using a coupled finite element formulation. The evaluation of the transport problem is performed based on the Galerkin Least Squares stabilized finite element method [8]. The stabilized approach eliminates potential instabilities resulting from the advection dominated flow generated around zones of stress concentration such as crack and notch tips.

The coupled solution of the deformation and transport problems are performed based on a staggered solution strategy of isothermal type. In this strategy, the mechanical and transport problems are evaluated in turn until convergence is achieved in both problems at each time step. When solving the transport problem, the pressure and the pressure gradients are considered as known fields, computed in the deformation problem. Similarly in the deformation problem, the concentration field is considered known computed in the evaluation of the transport problem at the current iteration. The thermal state of the system is regarded as an input to both transport and mechanical solvers. The thermal state of the structure is critical to the overall coupled chemo-mechanical deformation and failure behavior. The transient thermal diffusion, which is not modeled in this manuscript, may also be important in certain problems such as in the presence of high rate deformation. All cases in this manuscript investigate relatively long term behavior, in which isothermal conditions prevail (hours to hundreds of hours). The thermal steady state is typically reached in a matter of a few seconds, and therefore the thermal transients do not significantly affect the chemo-mechanical processes. A detailed formulation of the transport problem and the coupled solution algorithm has been provided in Ref. [36].

In the remainder of this section, a mixed finite element formulation is proposed and formulated for the viscoelastic-viscoplastic deformation model. In contrast to the traditional purpose of the mixed formulations (e.g., address incompressibility), the current formulation

employs the mixed approach to obtain an accurate description of the pressure and pressure gradient fields. The pressure and pressure gradient fields are in turn used to describe the advection and reaction components of the transport equation.

### 3.1 Recurrence formula for deviatoric stress tensor

A direct computation of the stress based on the viscoelastic strain (i.e., Eq. 11) requires the storage of and computation using the entire strain history. Storage of the entire strain history at each integration point within a large discretized domain is clearly expensive from the memory perspective. In order to reduce the memory cost, a recurrence formula has been employed [10]. Consider a time discretization of the governing deformation problem and let the left subscripts  $t$  denote the value of a response field at the previous equilibrated increment. Left subscripts  $t + \Delta t$  indicates the response field evaluated at the current increment. For simplicity, the left subscript for the current increment is sometimes omitted. From Eq. 12, the values of  $\boldsymbol{\varepsilon}$  at the previous and current increments are respectively:

$${}_t\varepsilon_{ij}^m = \int_0^t \exp\left(-\frac{t-\tau}{\xi_m}\right) \frac{d\varepsilon_{ij}^{\text{ve}}(\tau)}{d\tau} d\tau \quad (34)$$

$${}_{t+\Delta t}\varepsilon_{ij}^m = \int_0^t \exp\left(-\frac{t+\Delta t-\tau}{\xi_m}\right) \frac{d\varepsilon_{ij}^{\text{ve}}(\tau)}{d\tau} d\tau + \int_t^{t+\Delta t} \exp\left(-\frac{t+\Delta t-\tau}{\xi_m}\right) \frac{d\varepsilon_{ij}^{\text{ve}}(\tau)}{d\tau} d\tau \quad (35)$$

Assuming that the viscoelastic strain  $\boldsymbol{\varepsilon}^{\text{ve}}$  varies linearly within the current time step:

$${}_{t+\Delta t}\varepsilon_{ij}^m = \exp\left(-\frac{\Delta t}{\xi_m}\right) {}_t\varepsilon_{ij}^m + \frac{{}_{t+\Delta t}\varepsilon_{ij}^{\text{ve}} - {}_t\varepsilon_{ij}^{\text{ve}}}{\Delta t} \xi_m \left(1 - \exp\left(-\frac{\Delta t}{\xi_m}\right)\right) \quad (36)$$

Subtracting the deviatoric stress tensor evaluated at the previous and current time steps using Eq. 11, and employing Eq. 36 yields:

$$s_{ij} - {}_t s_{ij} = 2\bar{G} (\varepsilon_{ij}^{\text{ve}} - {}_t\varepsilon_{ij}^{\text{ve}}) \bar{K} - 2\bar{G} \sum_m^M K_m \left(1 - \exp\left(-\frac{\Delta t}{\xi_m}\right)\right) {}_t\varepsilon_{ij}^m \quad (37)$$

where,

$$\bar{K} = K_e + \sum_m^M K_m \left(1 - \exp\left(-\frac{\Delta t}{\xi_m}\right)\right) \frac{\xi_m}{\Delta t} \quad (38)$$

Equation 37 indicates that the calculation of the deviatoric stress at current time step requires the value of  $\boldsymbol{\varepsilon}$  at the previous time step, only rather than its entire history, significantly reducing the computing and memory requirements.

### 3.2 Mixed FEM formulation of the viscoelastic-viscoplastic deformation model

The weak forms of the governing equations of equilibrium in terms of the deviatoric stress and pressure (i.e., Eqs. 1 and 17, respectively) are expressed as:

$$\int_{\Omega} \nu_{i,j}^h s_{ij} d\Omega - \int_{\Omega} \nu_{i,i}^h p d\Omega - \int_{\Gamma_N^u} \nu_i^h \bar{t}_i d\Gamma - \int_{\Omega} \nu_i^h b_i d\Omega = 0 \quad (39)$$

$$\int_{\Omega} \frac{1}{k} q^h p^h d\Omega + \int_{\Omega} q^h u_{i,i}^h d\Omega - \int_{\Omega} 3q^h [\alpha (T - T_0) + \vartheta (c - c_{\infty})] d\Omega = 0 \quad (40)$$

where,  $\mathbf{v}$  and  $q$  are the test functions for displacement and pressure, defined within the appropriate Sobolev spaces and with sufficient smoothness. Let  $\mathbf{v}^h$  and  $q^h$  belong to the corresponding finite dimensional subspaces of the test functions,  $\mathbf{v}$  and  $q$ , respectively. We perform a Bubnov-Galerkin discretization of the displacement and pressure fields, as well as the corresponding test functions:

$$u_i^h(\mathbf{x}, t) = \sum_{a=1}^{n_u} N_a^u(\mathbf{x}) \hat{u}_{ai}(t) \quad (41)$$

$$p^h(\mathbf{x}, t) = \sum_{a=1}^{n_p} N_a^p(\mathbf{x}) \hat{p}_a(t) \quad (42)$$

in which,  $N_a^u$  and  $N_a^p$  are respectively the basis functions of the displacement and pressure fields that correspond to node  $a$ ;  $(\hat{\cdot})$  denotes the nodal coefficients of the corresponding field; and  $n_u$  and  $n_p$  are the total number of displacement and pressure nodes, respectively.

Substituting Eqs. 41 and 42 into Eqs. 39 and 40, respectively, the discretized equilibrium equations take the form:

$$\begin{aligned} \Psi_{bi} := & \int_{\Omega} N_{b,j}^u s_{ij} d\Omega - \sum_{c=1}^{n_p} \int_{\Omega} N_{b,i}^u N_c^p d\Omega \hat{p}_c - \int_{\Gamma_N^u} N_b^u \bar{t}_i d\Gamma \\ & - \int_{\Omega} N_b^u b_i d\Omega = 0; \quad b = 1, \dots, n_u \quad (43) \end{aligned}$$

$$\begin{aligned} \Theta_c := & \sum_{a=1}^{n_p} \int_{\Omega} \frac{1}{k} N_c^p N_a^p d\Omega \hat{p}_a + \sum_{b=1}^{n_u} \int_{\Omega} N_c^p N_{b,i}^u d\Omega \hat{u}_{bi} \\ & - \int_{\Omega} 3N_c^p [\alpha (T - T_0) + \vartheta (c - c_{\infty})] d\Omega = 0; \quad c = 1, \dots, n_p \quad (44) \end{aligned}$$

Consider a one-parameter family discretization of the viscoplastic strain rate in the form:

$$\frac{{}_t\!+\!\Delta t\dot{\varepsilon}_{ij}^{\text{VP}} - {}_t\dot{\varepsilon}_{ij}^{\text{VP}}}{\Delta t} = \theta {}_t\!+\!\Delta t\dot{\varepsilon}_{ij}^{\text{VP}} + (1 - \theta) {}_t\dot{\varepsilon}_{ij}^{\text{VP}} \quad (45)$$

in which,  $\theta \in [0, 1]$  is an algorithmic parameter. The choices of  $\theta = 0, 1$  and  $0.5$  correspond to the explicit, implicit and midpoint rules, respectively. Substituting Eqs. 5 and 41 into Eq. 37 and using Eq. 45, the discretized form of the constitutive equation for the deviatoric stress is expressed as:

$$\begin{aligned} R_{ij} := & {}_t\!+\!\Delta t s_{ij} - {}_t s_{ij} - 2\bar{G} \sum_{a=1}^{n_u} N_{a,j}^u(\mathbf{x}) {}_t\!+\!\Delta t \hat{u}_{ai} \bar{K} + 2\bar{G} \sum_{a=1}^{n_u} N_{a,j}^u(\mathbf{x}) {}_t \hat{u}_{ai} \bar{K} \\ & + 2\bar{G} \Delta t \theta {}_t\!+\!\Delta t \dot{\varepsilon}_{ij}^{\text{VP}} \bar{K} + 2\bar{G} \Delta t (1 - \theta) {}_t \dot{\varepsilon}_{ij}^{\text{VP}} \bar{K} + 2\bar{G} \sum_m^M K_m \left( 1 - \exp\left(-\frac{\Delta t}{\xi_m}\right) \right) {}_t \varepsilon_{ij}^m \end{aligned} \quad (46)$$

Equations 43, 44 and 46 together consist of the discretized nonlinear system of the viscoelastic-viscoplastic deformation problem. Newton's method is employed to solve this system of equations [15]. Considering the first order Taylor-series expansion of all three equations yield:

$$\begin{aligned} {}^{k+1}\Psi_{bi} & \approx {}^k\Psi_{bi} + \left( \frac{\partial \Psi_{bi}}{\partial s_{kl}} \right)^{k+1} \delta s_{kl} + \sum_{c=1}^{n_p} \left( \frac{\partial \Psi_{bi}}{\partial \hat{p}_c} \right)^{k+1} \delta \hat{p}_c \\ & = {}^k\Psi_{bi} + \int_{\Omega} N_{b,j}^u {}^{k+1} \delta s_{ij} d\Omega - \sum_{c=1}^{n_p} \int_{\Omega} N_{b,i}^u N_c^p d\Omega {}^{k+1} \delta \hat{p}_c = 0 \end{aligned} \quad (47)$$

$$\begin{aligned} {}^{k+1}\Theta_c & \approx {}^k\Theta_c + \sum_{b=1}^{n_u} \left( \frac{\partial \Theta_c}{\partial \hat{u}_{bk}} \right)^{k+1} \delta \hat{u}_{bk} + \sum_{a=1}^{n_p} \left( \frac{\partial \Theta_c}{\partial \hat{p}_a} \right)^{k+1} \delta \hat{p}_a \\ & = {}^k\Theta_c + \sum_{b=1}^{n_u} \int_{\Omega} N_c^p N_{b,i}^u d\Omega {}^{k+1} \delta \hat{u}_{bi} + \sum_{a=1}^{n_p} \int_{\Omega} \frac{1}{k} N_c^p N_a^p d\Omega {}^{k+1} \delta \hat{p}_a = 0 \end{aligned} \quad (48)$$

$$\begin{aligned} {}^{k+1}R_{ij} & \approx {}^k R_{ij} + \left( \frac{\partial R_{ij}}{\partial s_{kl}} \right)^{k+1} \delta s_{kl} + \sum_{a=1}^{n_u} \left( \frac{\partial R_{ij}}{\partial \hat{u}_{ak}} \right)^{k+1} \delta \hat{u}_{ak} \\ & = {}^k R_{ij} - 2\bar{G} \bar{K} \sum_{a=1}^{n_u} N_{a,j}^u {}^{k+1} \delta \hat{u}_{ai} + (I_{ijkl} + 2\bar{G} \bar{K} \theta \Delta t {}^k C_{ijkl}) {}^{k+1} \delta s_{kl} = 0 \end{aligned} \quad (49)$$

in which, the left superscript denotes the Newton iteration count. The Taylor series expansion is performed about the previous iteration,  $k$ .  $\delta(\cdot)$  denotes the incremental change in the

corresponding response field  $(\cdot)$  within the Newton iteration; and,

$${}^k C_{ijkl} = \left( \frac{\partial \dot{\varepsilon}_{ij}^{\text{vp}}}{\partial s_{kl}} \right) \quad (50)$$

The increment of deviatoric stress,  ${}^{k+1} \delta s_{ij}$  is evaluated using Eq. 49 as:

$${}^{k+1} \delta s_{ij} = {}^k Q_{ijkl} \left( 2\bar{G}\bar{K} \sum_{a=1}^{n_u} N_{a,l}^u {}^{k+1} \delta \hat{u}_{ak} - {}^k R_{kl} \right) \quad (51)$$

where, the modulus  ${}^k \mathbf{Q}$  is defined as:

$${}^k Q_{ijkl} = \left( I_{ijkl} + 2\bar{G}\bar{K}\theta\Delta t {}^k C_{ijkl} \right)^{-1} \quad (52)$$

Substituting Eq. 51 into Eqs. 47 and 48 yield:

$$\int_{\Omega} 2\bar{G}\bar{K} {}^k Q_{ijkl} N_{b,j}^u \sum_{a=1}^{n_u} N_{a,l}^u d\Omega {}^{k+1} \delta \hat{u}_{ak} - \sum_{c=1}^{n_p} \int_{\Omega} N_{b,i}^u N_c^p d\Omega {}^{k+1} \delta \hat{p}_c = \int_{\Omega} {}^k Q_{ijkl} N_{b,j}^u {}^k R_{kl} d\Omega - {}^k \Psi_{bi} \quad (53)$$

and,

$$- \sum_{b=1}^{n_u} \int_{\Omega} N_c^p N_{b,i}^u d\Omega {}^{k+1} \delta \hat{u}_{bi} - \sum_{a=1}^{n_p} \int_{\Omega} \frac{1}{k} N_c^p N_a^p d\Omega {}^{k+1} \delta \hat{p}_a = {}^k \Theta_c \quad (54)$$

Equations 53 and 54 are simultaneously evaluated for the increments of the displacement ( ${}^{k+1} \delta \hat{\mathbf{u}}$ ) and pressure fields ( ${}^{k+1} \delta \hat{\mathbf{p}}$ ) at the current iteration,  $k+1$ .

When expressed in the matrix form, Eqs. 53 and 54 yield:

$$\begin{bmatrix} {}^k \mathbf{K}^{uu} & \mathbf{K}^{up} \\ (\mathbf{K}^{up})^T & \mathbf{K}^{pp} \end{bmatrix} \begin{Bmatrix} {}^{k+1} \delta \hat{\mathbf{u}} \\ {}^{k+1} \delta \hat{\mathbf{p}} \end{Bmatrix} = \begin{Bmatrix} {}^k \mathbf{f}^u \\ {}^k \mathbf{f}^p \end{Bmatrix} \quad (55)$$

in which, the components of the tangent stiffness matrix are expressed as:

$${}^k K_{\alpha\beta}^{uu} = \int_{\Omega} 2\bar{G}\bar{K} {}^k Q_{ijmn} N_{b,j}^u \sum_{a=1}^{n_u} N_{a,n}^u d\Omega; \quad \alpha = b + (i-1)n_u; \quad \beta = a + (m-1)n_u \quad (56)$$

$$K_{\alpha c}^{up} = - \int_{\Omega} N_{b,i}^u N_c^p d\Omega; \quad \alpha = a + (i-1)n_u; \quad 1 \leq c \leq n_p \quad (57)$$

$$K_{ab}^{pp} = - \int_{\Omega} \frac{1}{k} N_a^p N_b^p d\Omega; \quad 1 \leq a, b \leq n_p \quad (58)$$

The left superscript is included only on the sub matrix,  $\mathbf{K}^{uu}$ , which is the only nonlinear part of the tangent stiffness. The unknown displacement and pressure coefficients, as well as the force vectors are expressed in the vector form as:

$${}^{k+1}\delta\hat{\mathbf{u}} = \{{}^{k+1}\hat{u}_1, \dots, {}^{k+1}\hat{u}_{n_{sd} \times n_u}\}^T; \quad {}^k\mathbf{f}^u = \{{}^k f_1^u, \dots, {}^k f_{n_{sd} \times n_u}^u\}^T \quad (59)$$

$${}^{k+1}\delta\hat{\mathbf{p}} = \{{}^{k+1}\hat{p}_1, \dots, {}^{k+1}\hat{p}_{n_p}\}^T; \quad {}^k\mathbf{f}^p = \{{}^k f_1^p, \dots, {}^k f_{n_p}^p\}^T \quad (60)$$

and the components of the force vector are given as:

$${}^k f_\alpha^u = \int_{\Omega} {}^k Q_{ijkl} N_{b,j}^u {}^k R_{kl} d\Omega - {}^k \Psi_{bi}; \quad \alpha = b + (i - 1) n_u \quad (61)$$

$${}^k f_a^p = {}^k \Theta_a; \quad 1 \leq a \leq n_p \quad (62)$$

The finite elements discretizing the displacements and the pressure fields are chosen in order to satisfy the Babuska-Brezzi constraint. Ensuring this constraint is satisfied in the choice of the pressure and displacement discretizations avoids the potential numerical instability and response oscillations observed in mixed formulations. In the numerical studies provided in this manuscript, we employ nine-node biquadratic in displacement and four-node bilinear in pressure Taylor-Hood element.

Based on the expressions above, we employ the following algorithm to compute the pressure and displacement fields:

*At arbitrary time  $t + \Delta t$ :* Given the state at the previous time step;  ${}_t\hat{\mathbf{u}}$ ,  ${}_t\hat{\mathbf{p}}$ ,  ${}_t\mathbf{s}$  and  ${}_t\dot{\boldsymbol{\epsilon}}^{vp}$ ; Find the response at the current step;  $\hat{\mathbf{u}}$ ,  $\hat{\mathbf{p}}$ .

1. Initiate the algorithm:  $k = 0$ .
2. Set the initial guesses for the pressure and deformation coefficients at the current increment:

$${}^0\hat{\mathbf{u}} = {}_t\hat{\mathbf{u}}; \quad {}^0\hat{\mathbf{p}} = {}_t\hat{\mathbf{p}}; \quad {}^0\mathbf{s} = {}_t\mathbf{s}; \quad {}^0\dot{\boldsymbol{\epsilon}}^{vp} = {}_t\dot{\boldsymbol{\epsilon}}^{vp} \quad (63)$$

3. Loop until convergence:
  - (a) Compute the moduli:  $\bar{K}$ ,  ${}^k\mathbf{C}$  and  ${}^k\mathbf{Q}$  using Eqs. 38, 50 and 52, respectively.
  - (b) Calculate  ${}^k\boldsymbol{\Psi}$ ,  ${}^k\boldsymbol{\Theta}$  and  ${}^k\mathbf{R}$  using Eqs. 43, 44 and 46, respectively.
  - (c) Update the pressure and displacement increments,  ${}^{k+1}\delta\hat{\mathbf{u}}$  and  ${}^{k+1}\delta\hat{\mathbf{p}}$  by solving the linear system in Eq. 55.
  - (d) Compute deviatoric stress increment  ${}^{k+1}\delta\mathbf{s}$  at each integration point using Eq. 51.

(e) Update displacement, pressure and stress:

$${}^{k+1}\hat{\mathbf{u}} = {}^{k+1}\delta\hat{\mathbf{u}} + {}^k\hat{\mathbf{u}} \quad (64)$$

$${}^{k+1}\hat{\mathbf{p}} = {}^{k+1}\delta\hat{\mathbf{p}} + {}^k\hat{\mathbf{p}} \quad (65)$$

$${}^{k+1}\mathbf{s} = {}^{k+1}\delta\mathbf{s} + {}^k\mathbf{s} \quad (66)$$

(f) Update  ${}^{k+1}\dot{\boldsymbol{\epsilon}}^{\text{vp}}$  and  ${}^{k+1}\boldsymbol{\epsilon}^{\text{vp}}$  by simultaneously evaluating:

$${}^{k+1}\boldsymbol{\epsilon}^{\text{vp}} = {}_t\boldsymbol{\epsilon}^{\text{vp}} + \theta\Delta t {}^{k+1}\dot{\boldsymbol{\epsilon}}^{\text{vp}} + (1 - \theta)\Delta t {}_t\dot{\boldsymbol{\epsilon}}^{\text{vp}} \quad (67)$$

$${}^{k+1}\dot{\boldsymbol{\epsilon}}^{\text{vp}} = \gamma \left\langle \frac{{}^{k+1}f}{{}^{k+1}\sigma_Y} \right\rangle^q {}^{k+1} \left( \frac{\partial f}{\partial \boldsymbol{\sigma}} \right) \quad (68)$$

(g)  $k = k + 1$

## 4 Numerical Investigation of Ti-6242S Response in Combined Environment

The proposed computational model was employed to investigate the mechanical response of a titanium alloy exposed to oxygen at elevated temperatures. We focus on modeling the near alpha titanium alloy, Ti-6Al-2Sn-4Zr-2Mo-0.1Si (Ti-6242S) within a temperature range of 23-650°C. Ti-6242S displays good mechanical properties at elevated temperature, making them a candidate structural material for hypersonic aircraft applications. The applicability of the proposed model to idealize the behavior of the alloy requires temperature stability, since the effect of microstructure evolution is not explicitly included. The tensile strength properties of Ti-6242S have been reported to be largely unaffected at creep - high temperature exposure conditions up to 650°C [31]. While the micrographs of from the experimental investigations considered in this study is not available, the literature on prior experiments and imaging performed on aged specimens at temperatures up to 650°C points to limited microstructure evolution (see e.g., [22]). It is possible that even higher temperatures would induce microstructural evolution that will significantly alter the physical mechanisms that shape the relaxation, creep and other mechanical behavior of this alloy. It is noted that the maximum temperature covered in this study already extends the range of temperatures considered in applications of Ti-6242S, which is typically limited to 500-550°C. Nevertheless, a more systematic experimental study is needed to clarify the sources of high temperature deformation mechanisms, including the microstructure evolution.

The present investigation includes the calibration of the model parameters for the chosen titanium alloy based on experimental data (Section 4.1), and characterization of the

Table 1: Material parameters for oxygen transport in Ti-6Al-2Sn-4Zr-2Mo-0.1Si.

$D_0$ [mm <sup>2</sup> /s]	$c_\infty$ [%]	$Q$ [kJ/mole]	$\omega_c$	$\omega_{ec}$	$a$	$V_O$ [cm <sup>3</sup> /mole]
5.397	0.15	184.8	0.1	0.7	3.56	3.5

Table 2: Material parameters for viscoplastic deformation of Ti-6Al-2Sn-4Zr-2Mo-0.1Si.

$\nu$	$E_0$ [GPa]	$\gamma$ [MPa/h]	$\dot{\epsilon}^0$ [1/s]	$\alpha$ [1/°C]	$\vartheta$ [1/%c]	$A$ [MPa]
0.32	120.8	2000.0	1.0	7.7e-6	1.1e-3	895.0
$B$ [MPa]	$F$ [MPa/%c]	$n$	$m$	$c_{\text{crit}}$ [%]	$T_\beta$ [°C]	$q_{\text{ref}}$
125.0	140.0	0.2	1.35	4.5	1000.0	1.0
$\bar{q}$	$D_1^\infty$	$D_1^\alpha$	$D_5$	$D_6$	$M$	$K_e$
2.7586	0.1676	5.0e-3	9.5e-7	23.25	5	0.0
$K_1$	$K_2$	$K_3$	$K_4$	$K_5$	$\xi_1$ [h]	$\xi_2$ [h]
0.5	0.2	0.15	0.1	0.05	4.5e4	4.667e5
$\xi_3$ [h]	$\xi_4$ [h]	$\xi_5$ [h]	$C_1$	$C_2$		
4.167e6	4.167e7	4.167e8	-6.3714	-1094.75		

coupling effects between the oxygen embrittlement, viscous and deformation mechanisms (Section 4.2).

## 4.1 Model calibration

Model calibration includes the identification of the material properties for oxygen transport into the titanium alloy, the viscoelastic and viscoplastic properties of the alloy as well as the properties that characterize the coupling between the transport and deformation processes. Model calibration is performed based on the experimental data conducted at the Air Force Research Laboratory, as well as the data available in the literature. The calibrations that include multiple model parameters were conducted using the least squares minimization of the pertinent objective function, defined as the discrepancy between the experimental observable (e.g., stress-strain curve, relaxation curve, etc.) and the results of the numerical simulations.

The calibrated oxygen transport model parameters are summarized in Table 1. The pre-exponential constant,  $D_0$ , and the activation energy,  $Q$ , are experimentally determined as 5.397 mm<sup>2</sup>/s and 184.8 kJ/mole, respectively. These parameters are consistent with prior experimental investigations [17, 33] as well. The bulk oxygen concentration in the titanium alloy is provided by the manufacturer (Timet) as 0.15%. The partial molar volume of oxygen in the alloy is taken to be 3.5 cm<sup>3</sup>/mole, same as that reported by Ref. [35] for pure titanium. The parameters that characterize the effect of mechanical damage on oxygen diffusivity,  $\omega_c$ ,  $\omega_{ec}$  and  $a$  are consistent with the reported values based on the percolation theory [1, 20].

The material properties that describe the mechanical behavior are summarized in Table 2.

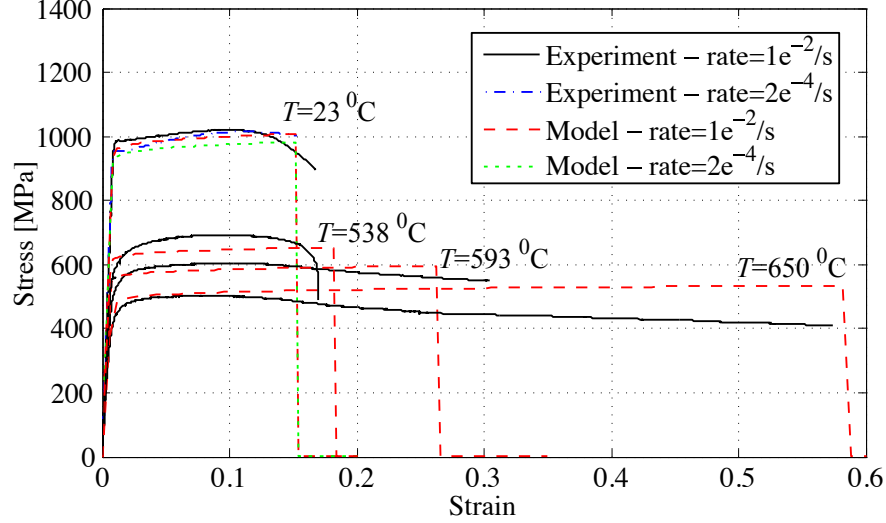


Figure 3: The stress-strain response of Ti-6Al-2Sn-4Zr-2Mo-0.1Si at room and elevated temperatures.

The temperature effect on the elastic and plastic responses are calibrated based on a series of uniaxial tensile experiments conducted at room temperature,  $538^{\circ}\text{C}$ ,  $593^{\circ}\text{C}$  and  $650^{\circ}\text{C}$ , from which the temperature variation of Young's modulus, Poisson's ratio, yield strength, failure strain and strain hardening variable are calibrated. The loading rate effect is investigated at room temperature only, where the viscosity at room temperature was determined. The loading rate experiment conducted at room temperature shows little difference between the fast and slow loading tests. The rate effect is typically stronger at elevated temperatures and the discrepancy between the fast and slow loading tests could be more pronounced. Literature on the quantified effect of load rate on the yield strength at high temperature for Ti-6242S is quite limited and additional experimental data to fully quantify the rate effects is needed. The simulated stress-strain response at high temperatures using the calibrated properties are compared to the experimental measurements in Fig. 3. The necking process dictated by large structural deformation is not incorporated into the proposed model and currently the model is limited to small deformation theory. No attempt was therefore made to calibrate the post-peak behavior of the engineering curve. The oxygen induced hardening parameter,  $F$ , is calibrated based on the microhardness experiments conducted on oxygen-exposed specimens [26]. The embrittlement parameter,  $D_1^{\alpha}$ , is chosen such that the ductility nearly vanishes at the critical oxygen concentration  $c_{crit}$ , taken to be 4.5%. The resulting constitutive response as a function of concentration are illustrated in Figs. 4 and 5 at room temperature and  $593^{\circ}\text{C}$ , respectively.

The viscoplastic parameters including the fluidity parameter,  $\gamma$ , the viscoplastic hardening parameters,  $q_0$  and  $q^*$ , and the viscoelastic parameters including the number of Maxwell

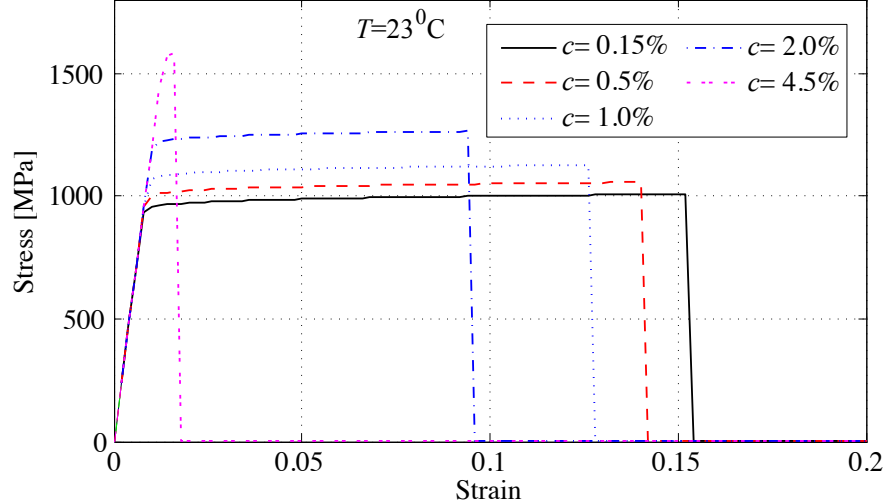


Figure 4: The stress-strain response of Ti-6Al-2Sn-4Zr-2Mo-0.1Si with varying oxygen content at room temperature.

elements,  $M$ , the Prony series coefficients,  $K_m$  and  $\xi_m$  ( $m = 1, \dots, M$ ), and the temperature dependence parameters,  $C_1$  and  $C_2$ , are calibrated based on stress relaxation tests conducted at temperatures of  $593^\circ\text{C}$  and  $650^\circ\text{C}$ . The number of Maxwell elements is chosen as 5, the minimum number necessary to accurately evaluate the stress relaxation response at both short and long time scales. Figure 6 compares the experimentally observed and simulated short term relaxation behavior at temperatures of  $593^\circ\text{C}$  and  $650^\circ\text{C}$  under the constant strain magnitude of 3.5%. Within the first 40 seconds of relaxation, both viscoelastic and viscoplastic relaxation processes are active since the specimens were loaded to stress levels beyond the static yield strength. Figures 7 and 8 compare the simulated and observed long-term relaxation behavior up to 100 hours. The long-term relaxation behavior is governed by the viscoelastic component of the model only, as the stress drops below the temperature dependent static yield stress. A near complete relaxation is observed at 100 hours of exposure of the specimen to  $650^\circ\text{C}$ , whereas the stress asymptotes at approximately 6.25 MPa when exposed to  $593^\circ\text{C}$ . In both cases, the model is in excellent agreement with the observed relaxation behavior. Further experimental investigation of the microstructure during the combined loading and high temperature exposure would provide additional information on the microstructural origins of the relaxation process. The relaxation experiments included in this study were uninterrupted and the possible microstructure evolution was therefore could not be observed.

## 4.2 Response under combined thermo-mechanical environment

The calibrated transport-deformation model is employed to investigate the combined environment response of Ti-6242S. The investigations focused on the coupling mechanisms

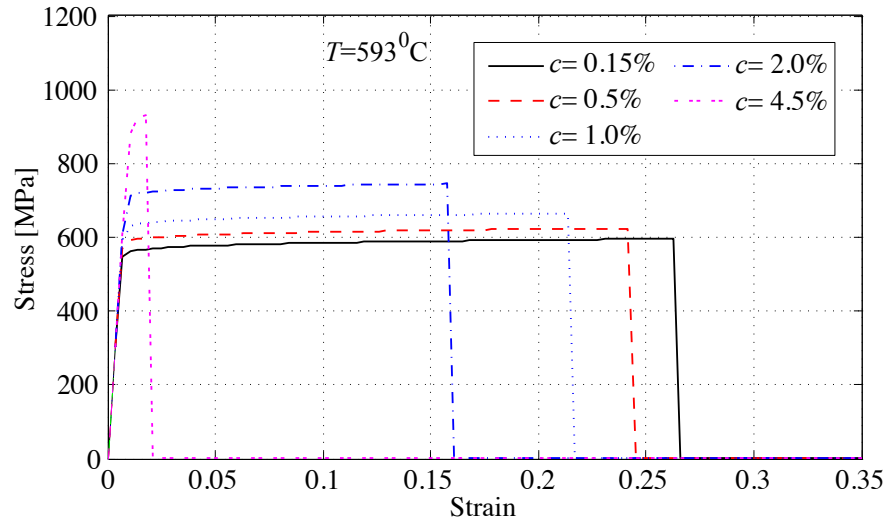


Figure 5: The stress-strain response of Ti-6Al-2Sn-4Zr-2Mo-0.1Si with varying oxygen content at 593 °C.

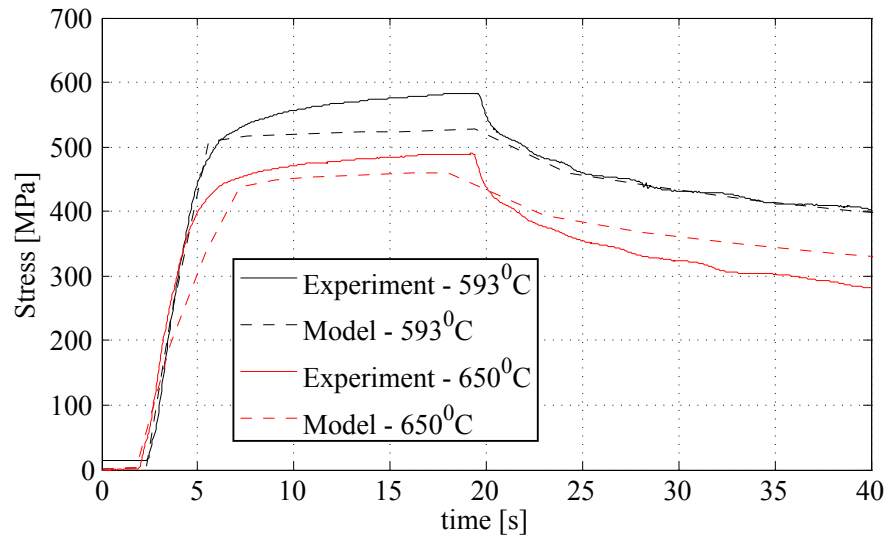


Figure 6: The stress relaxation test of Ti-6Al-2Sn-4Zr-2Mo-0.1Si at 593°C and 650°C for 40 seconds.

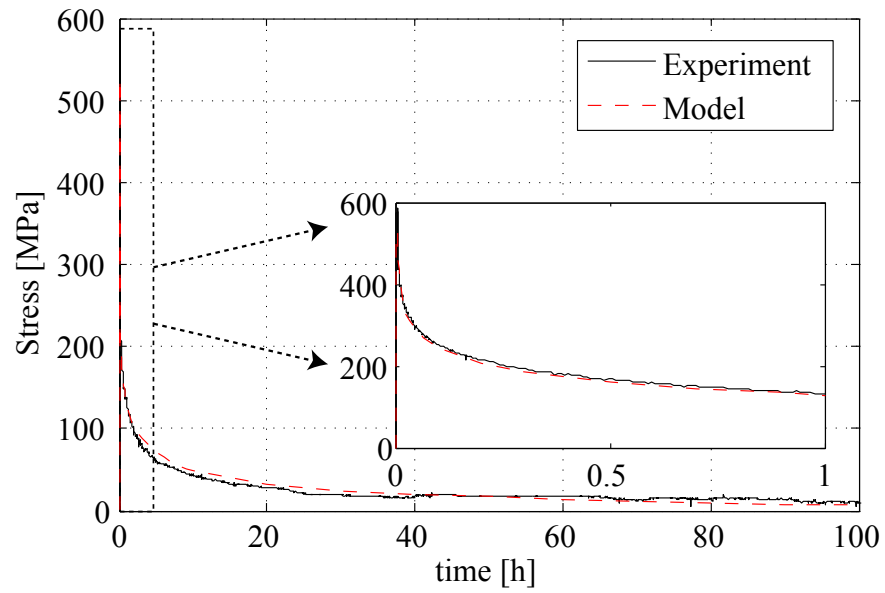


Figure 7: The stress relaxation test of Ti-6Al-2Sn-4Zr-2Mo-0.1Si at 593<sup>0</sup>C for 100 hrs.

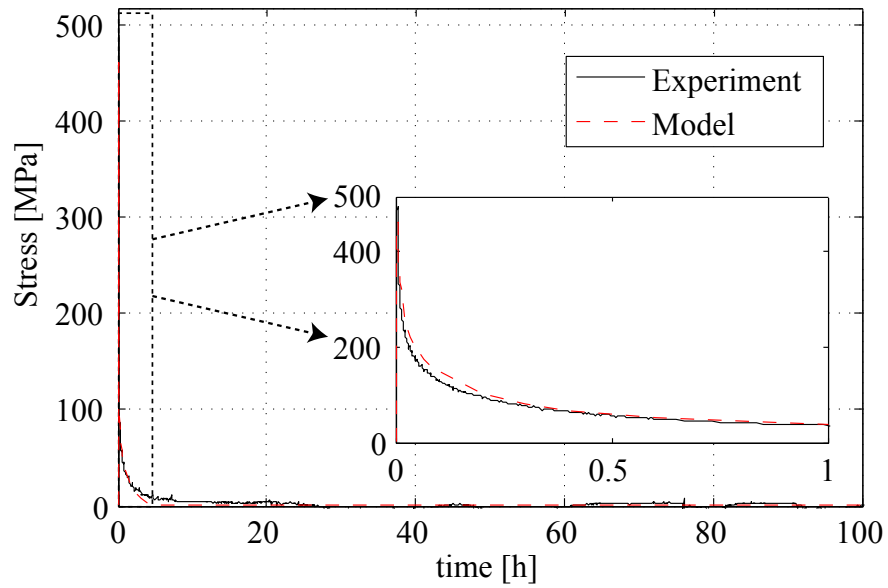


Figure 8: The stress relaxation test of Ti-6Al-2Sn-4Zr-2Mo-0.1Si at 650<sup>0</sup>C for 100 hrs.

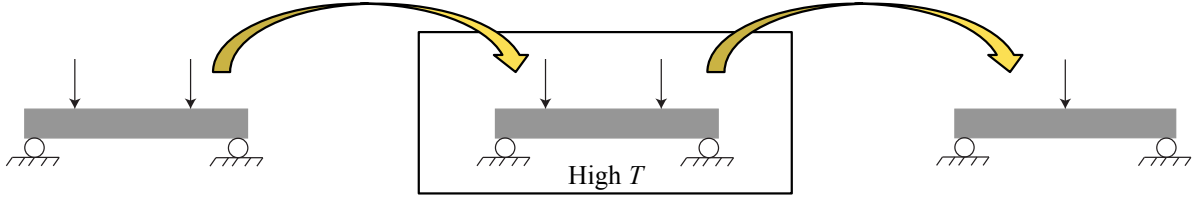


Figure 9: Coupled transport- deformation experiments procedure

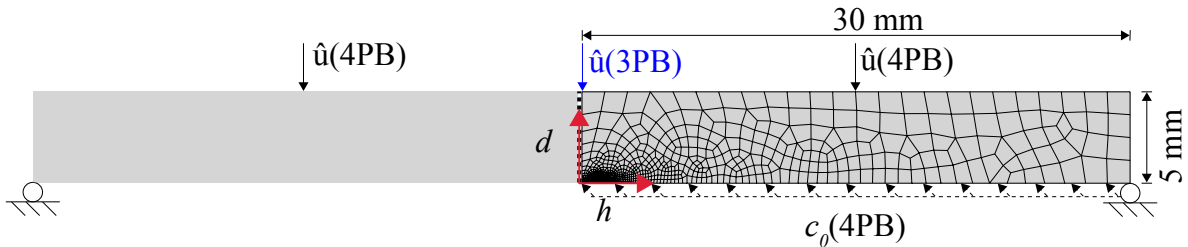


Figure 10: Geometry, boundary condition and finite element mesh of the 4 point bend and the 3 point bend configurations.

between oxygen transport, relaxation and deformation behavior. The proposed numerical investigations are focused on the combined environment setup of the experiments conducted by Peters *et al.* [27]. Figure 9 illustrates the overview of the experimental procedure. Each specimen was displacement-loaded using four-point bend (4PB) apparatus. The specimens were consequently subjected to constant elevated temperature at their loaded state. The duration of high temperature exposure was 100 hours. The specimens were then cooled back to the room temperature and tested using a three-point bend (3PB) setup. Four different scenarios were considered: specimens subjected to 0.75mm (low amplitude loading) or 1.5mm (high amplitude loading) maximum displacement in 4PB apparatus and exposed to 450°C and 550°C in the heating chamber.

Figure 10 shows the geometry, boundary conditions and the finite element discretization of the numerical specimen. Plane-strain conditions were assumed. Only half of the specimen is discretized due to the symmetry of the geometry and the loading conditions. For computational efficiency, the focus is kept on the tension (bottom) side of the specimen. The bottom-left corner of the specimen has very fine resolution with element size of approximately 0.2 $\mu$ m. The oxygen ingress is applied at the tension side only since the oxygen induced tension cracks are more critical than the compression observed at the top surface.

Table 3 summarizes the maximum stress achieved immediately after loading in specimens subjected to four-point bending at elevated temperatures. The computed values are compared to theoretical maximum stress provided in Ref. [27]. The computed and theoretical stress magnitudes are in reasonable agreement with each other, albeit some differences particularly at high loading amplitude. The discrepancy is attributed to the fact that the

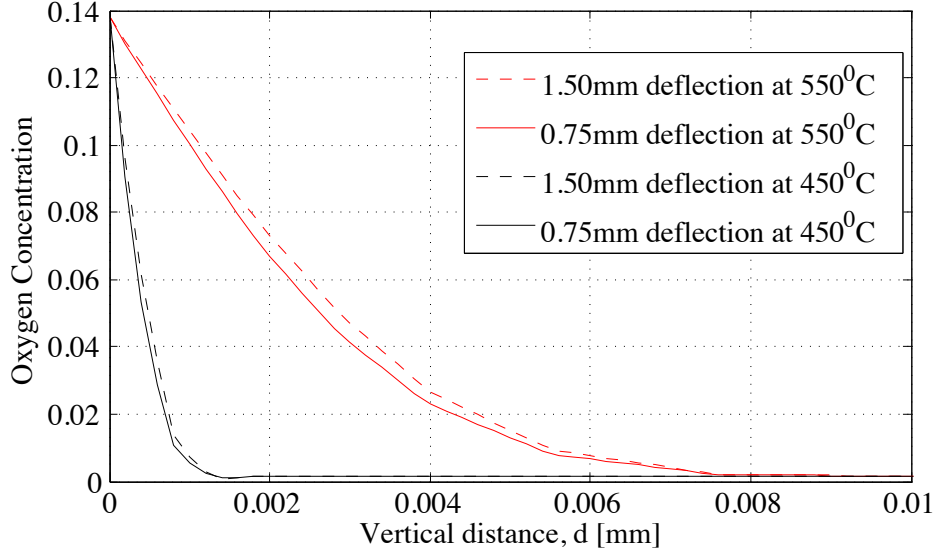


Figure 11: Oxygen concentration along the depth from the tensile surface.

theoretical values do not consider relaxation during the loading process. The low amplitude loading remains within the elastic range at both  $450^{\circ}\text{C}$  and  $550^{\circ}\text{C}$ . Figure 11 shows the oxygen concentration distribution measured from the center of the bottom surface along the vertical direction towards the interior for all four configurations after the 100 hour high temperature exposure. The oxygen content of the ambient environment is taken to be 13.8% wt. [26], which was applied as the concentration boundary condition at the tension side of the specimen. We note that the oxygen uptake capacity of the alloy is approximately 7% wt. beyond which the oxide layer is formed [32]. Typically, the size of the oxide layer is significantly smaller than the oxygen enriched case and the effects of oxide formation are neglected. Figure 11 shows that the presence of loading has a nominal effect on the oxygen ingress in this case, which is consistent with the experimental observations. The thicknesses of the oxygen enriched layers are  $3.162\ \mu\text{m}$ ,  $2.868\ \mu\text{m}$ ,  $0.588\ \mu\text{m}$  and  $0.515\ \mu\text{m}$  for the high load -  $550^{\circ}\text{C}$ , low load -  $550^{\circ}\text{C}$ , high load -  $450^{\circ}\text{C}$  and low load -  $450^{\circ}\text{C}$  cases, respectively. Since there is no significant inelastic strain in the low amplitude load cases, the mechanical state does not affect the oxygen ingress.

#### 4.2.1 Relaxation and oxygen ingress under high temperature exposure

Since the four point bending tests were performed at high temperatures under displacement control, significant stress relaxation is expected. The relaxation process interacts with both the transport of oxygen and the resulting stress state. Figure 12 shows the equivalent stress history at the bottom center of the specimen for the four test conditions. The specimens loaded at low applied displacement magnitude display a typical relaxation behavior. Since no plastic deformation is predicted at low amplitude loading, the relaxation is entirely vis-

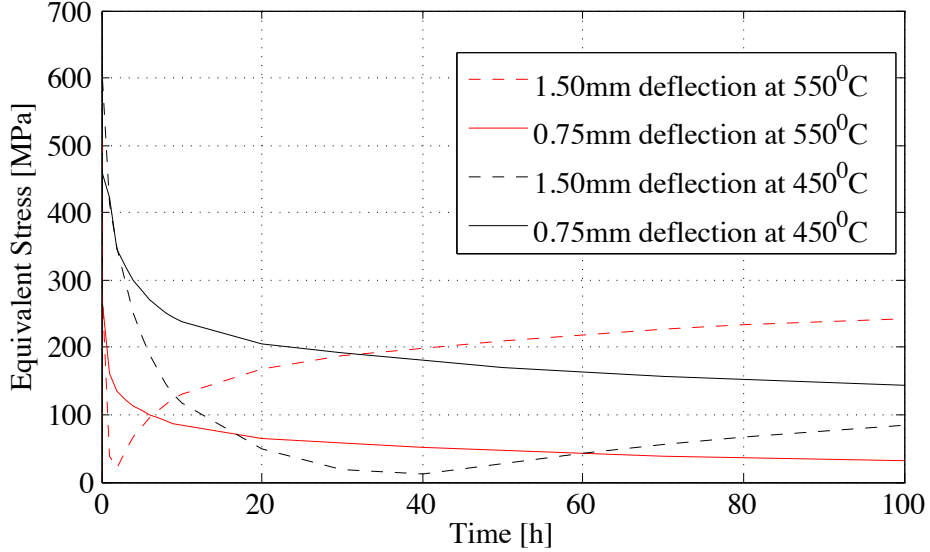


Figure 12: Equivalent stress variation in 4 point bending tests for 100 h at the center of the tensile surface.

coelastic. At high amplitude loading, a very different stress evolution is observed at both temperatures, in which an exponential relaxation is followed by a stress recovery phase. For instance, at 550°C, the stress drops from the peak value of 513 MPa to 38 MPa after 1 hour and steadily increase to 243 MPa at 100 hours of exposure. At 450°C, the stress recovery behavior is similar to the 550°C case, but the recovery is less severe.

In order to interpret the stress recovery observed in plastically loaded specimens, the numerical simulations were extended up to 2000 hours of high temperature exposure, at which the specimens reach full relaxation or steady state. Figure 13 depicts the equivalent stress distribution of the four point bending specimens along the vertical line measured from the bottom-center towards the top (shown as vector  $d$  in Fig. 10) at a number of time instances. When the midspan deflection is set to 0.75 mm (i.e., low amplitude loading) the stresses relax uniformly as the process is purely viscoelastic as shown in Fig. 13a,b. The specimen subjected to 550°C displays complete relaxation at the exposure time of 2000 hr. The slight stress asymmetry between the compression and tension sides is due to the biased meshing as well as the oxygen ingress imposed on the tension side. When the specimens are plastically loaded with midspan deflection of 1.5mm, a significantly different time dependent behavior is observed as shown in Fig. 13c,d. The loading clearly induces plastic deformation near the compression and tension sides of the specimens with approximately 1 mm thickness. Within the interior of the specimens, the deformation remains viscoelastic. Initially, the plastically loaded region induces a faster relaxation compared to the elastically loaded region since both the viscoelastic and viscoplastic stress relaxation mechanisms are active in the plastically loaded region. The uneven relaxation moves the peak stress towards the interior of the

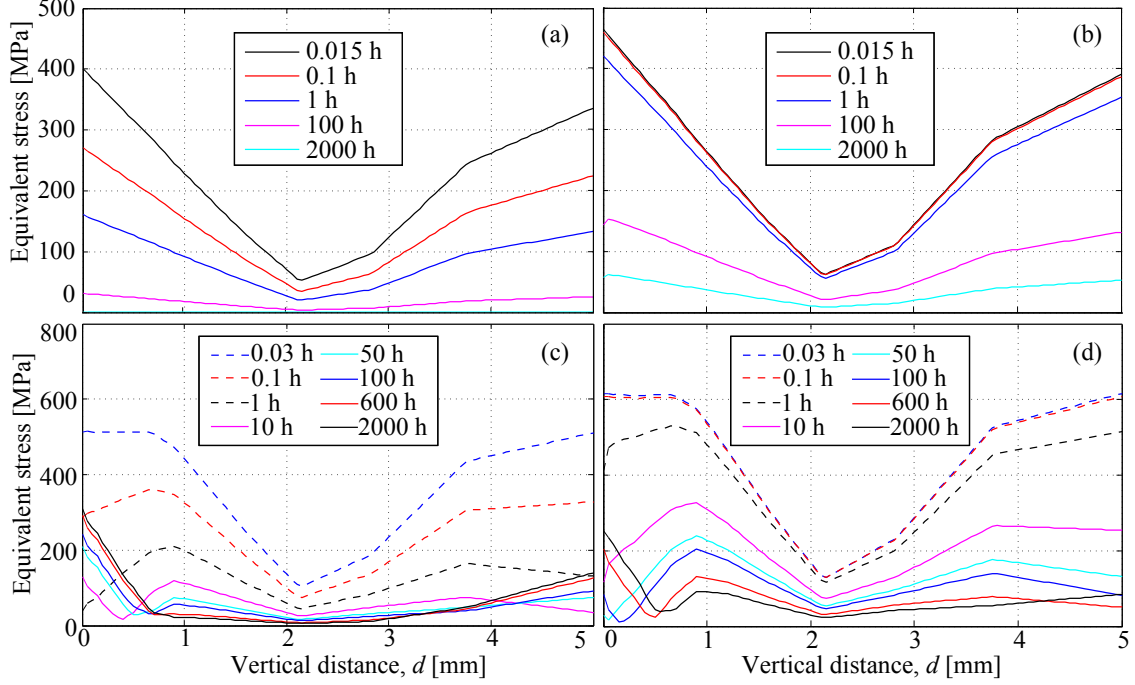


Figure 13: Equivalent stress along the depth from the tensile surface: (a) 0.75 mm loading at 550<sup>0</sup>C; (b) 0.75 mm loading at 450<sup>0</sup>C; (c) 1.5 mm loading at 550<sup>0</sup>C; and (d) 1.5 mm loading at 450<sup>0</sup>C.

specimen. The relaxation induced stress distribution is resisted by the equilibrium process, which leads to higher stresses at the outer faces of the specimen at longer times. At the steady state, significant residual stresses are observed at the plastically loaded outer faces of the specimens. It is important to note that the stress recovery process is limited to the outer faces of the specimen and despite the stress recovery mechanism, the overall energy of the specimen monotonically reduces during the exposure duration since the viscous dissipation process is not recoverable. Similar behavior is observed in the specimens subjected to 550<sup>0</sup>C and 450<sup>0</sup>C environments. The relaxation and stress recovery naturally occurs at a faster rate at 550<sup>0</sup>C (Fig. 13c) compared to 450<sup>0</sup>C (Fig. 13d). The time evolution of the stress contours within the four-point bending tests under 550<sup>0</sup>C exposure for the elastically and plastically loaded specimens are shown in Fig. 14. The spatial evolution of the equivalent stress in the plastically loaded specimens are highly nonuniform in contrast to the elastically loaded specimens, whose stress distribution remains nearly identical with monotonically decreasing magnitude.

#### 4.2.2 Three-Point Bend Response of Exposed Specimens

The numerical specimens subjected to 100 hours of high temperature exposure at the loaded state are unloaded and cooled to the room temperature prior to further testing using the

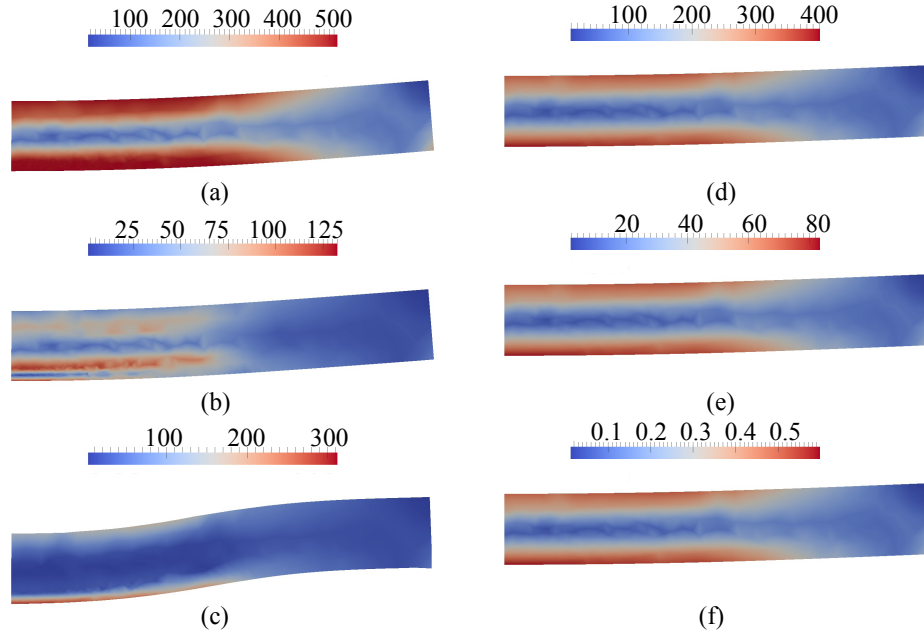


Figure 14: Equivalent stress contour of 4 point bending specimen at 550<sup>0</sup>C with: (a) 1.50 mm midspan deflection at 0.03 hr; (b) 1.50 mm midspan deflection at 10 hrs; (c) 1.50 mm midspan deflection at 2000 hrs; (d) 0.75 mm midspan deflection at 0.015 hr; (e) 0.75 mm midspan deflection at 10 hrs; (f) 0.75 mm midspan deflection at 2000 hrs;

Table 3: Influence of oxidation on cracking at room temperature in 3-P bending.

T (°C)	D (mm)	4PB		3PB	
		$\sigma_{\max}$ [MPa] Theoretical [27]	$\sigma_{\max}$ [MPa] Model	[cracks/mm] Experiment	[cracks/mm] Model
450	0.75	419.00	464.64	-	18.18
450	1.50	$>644.20(\sigma_{p0.2})$	619.80	20.00	$18.18 \pm 9.1\%$
550	0.75	390.00	400.66	22.36	$18.18 \pm 18.7\%$
550	1.50	$>578.80(\sigma_{p0.2})$	516.73	8.70	$10.26 \pm 17.9\%$

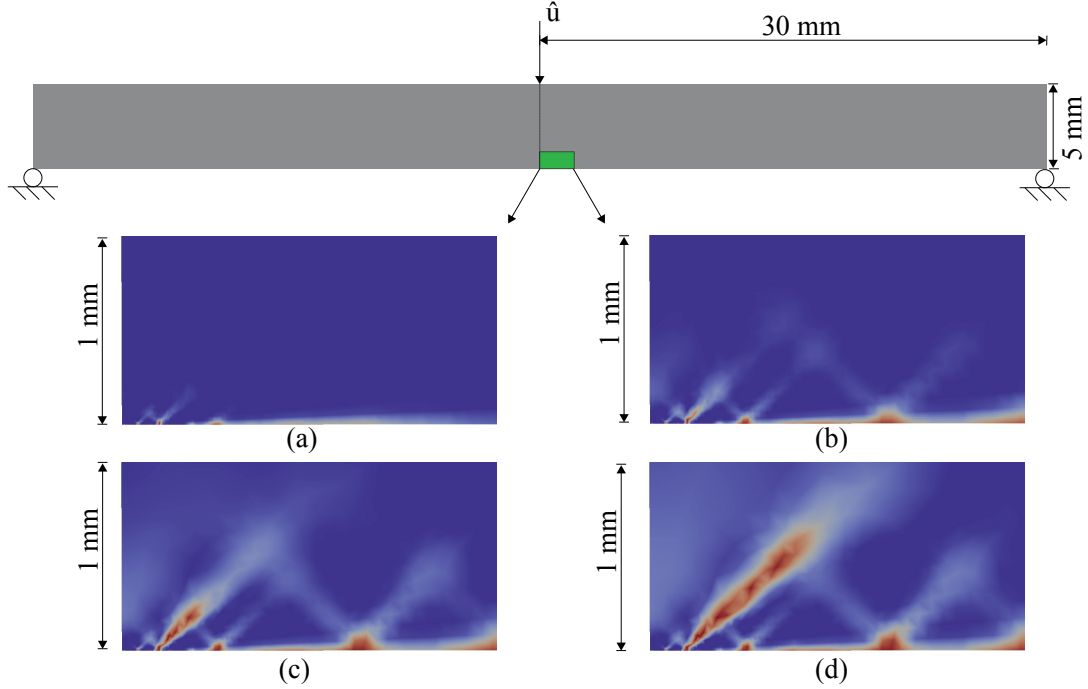


Figure 15: Three point bending damage at applied displacement of: (a) 2.4 mm; (b) 2.9 mm; (c) 3.3 mm; (d) 3.7 mm of the specimen oxidized with 0.75 mm deflection at 450<sup>o</sup>C.

three-point bend test setup. This procedure mimics the experimental protocol followed by Peters *et al.* [27]. A midpoint vertical deflection of up to 3.6 mm and 4.8 mm was applied to the specimens exposed to 550<sup>o</sup>C and 450<sup>o</sup>C environment, respectively.

Figure 15 displays the damage propagation during the 3PB testing of the specimen that was exposed to 450 <sup>o</sup>C under the midspan deflection of 0.75 mm. The damage contours are from a 2mm by 1mm region near the central section of the tensile surface. A thin surface layer of 0.515  $\mu\text{m}$  thickness has reached or exceeded  $c_{crit}$  during the exposure process, within which the early onset of damage propagation is initiated. The damage progressively propagates towards the interior of the specimen along the shear path, reaching a length of 0.8 mm at the applied midspan deflection of 3.7 mm. The damage evolution during the 3PB testing of the specimen that was exposed to 450 <sup>o</sup>C under the midspan deflection of 1.5 mm is very similar, which indicates that the small change in the surface oxygen concentration has insignificant effect on the mechanical performance. Figure 16 compares the damage state in the three-point bend specimens subjected to 3.6 mm midspan deflection, that were previously exposed to 550 <sup>o</sup>C under the midspan deflection of 0.75 mm and 1.5 mm. The specimen that was previously exposed to high temperature while viscoelastically loaded developed a slightly larger damage region compared to the viscoplastically loaded specimen. The difference between the oxygen enriched region thicknesses between the two specimens prior to the three-point bending is nominal, whereas the initial stress distributions are significantly

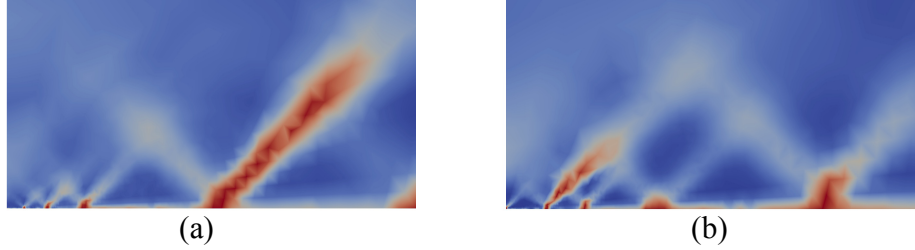


Figure 16: Three point bending damage at applied displacement of 3.6 mm of the specimen oxidized at 550<sup>0</sup>C with deflection: (a) 0.75 mm; (b) 1.50 mm.

different owing to the stress recovery process discussed above. The discrepancy between the damage patterns is attributed to the different stress states of the specimens prior to loading in the three-point bend apparatus. In both cases shown in Fig. 16, the cracks propagate at an angle of approximately 41<sup>0</sup>-45<sup>0</sup>. Experimental data on the direction of the crack paths is not available for validation of the path of crack propagation, which may shed further light on the microstructural origins of the failure behavior.

In the current manuscript, the scalar damage variable affects the behavior only at the onset of the state of failure (i.e.,  $\omega = 1$ ). At failure, the residual stiffness of the corresponding element is set to a small fraction of the elastic stiffness of the material, which accounts for failure induced relaxation and load redistribution. The stiffness relaxation introduced by this approach is known to induce mesh-dependency [2, 7]. Introduction of advection-diffusion terms was shown to regularize mesh dependency in certain conditions [21, 37]. Through a similar mechanism, the coupling between the oxygen transport and the deformation problem could pose as localization limiter of the deformation problem. The results in this study indicate that the mesh localization phenomenon is not observed and the damage zone thickness remains larger than the mesh size (3 $\times$  the element size) in the example problems studied herein. The current manuscript does not include a thorough mesh localization investigation and further study of this point is needed to assess whether realistic oxygen diffusion rates could act as localization limiter for the deformation problem.

Figure 17 displays the three point bending damage profiles along the tensile surface for specimens previously exposed to 450<sup>0</sup>C and 550<sup>0</sup>C. The three point bending test generates nearly identical damage distribution along the tensile surface within the specimens previously subjected to 450<sup>0</sup>C regardless of the four point bend loading amplitude as shown in Fig. 17a-c. In contrast, the specimen previously subjected to 550<sup>0</sup>C and low four point bend loading amplitude has a significantly different surface damage pattern compared to the specimen previously subjected to 550<sup>0</sup>C and high four point bend loading amplitude as shown in Fig. 17d-f. One key difference is the change in the periodic crack spacing, which reduces from approximately 18 cracks/mm to 10 cracks/mm, which is consistent with the

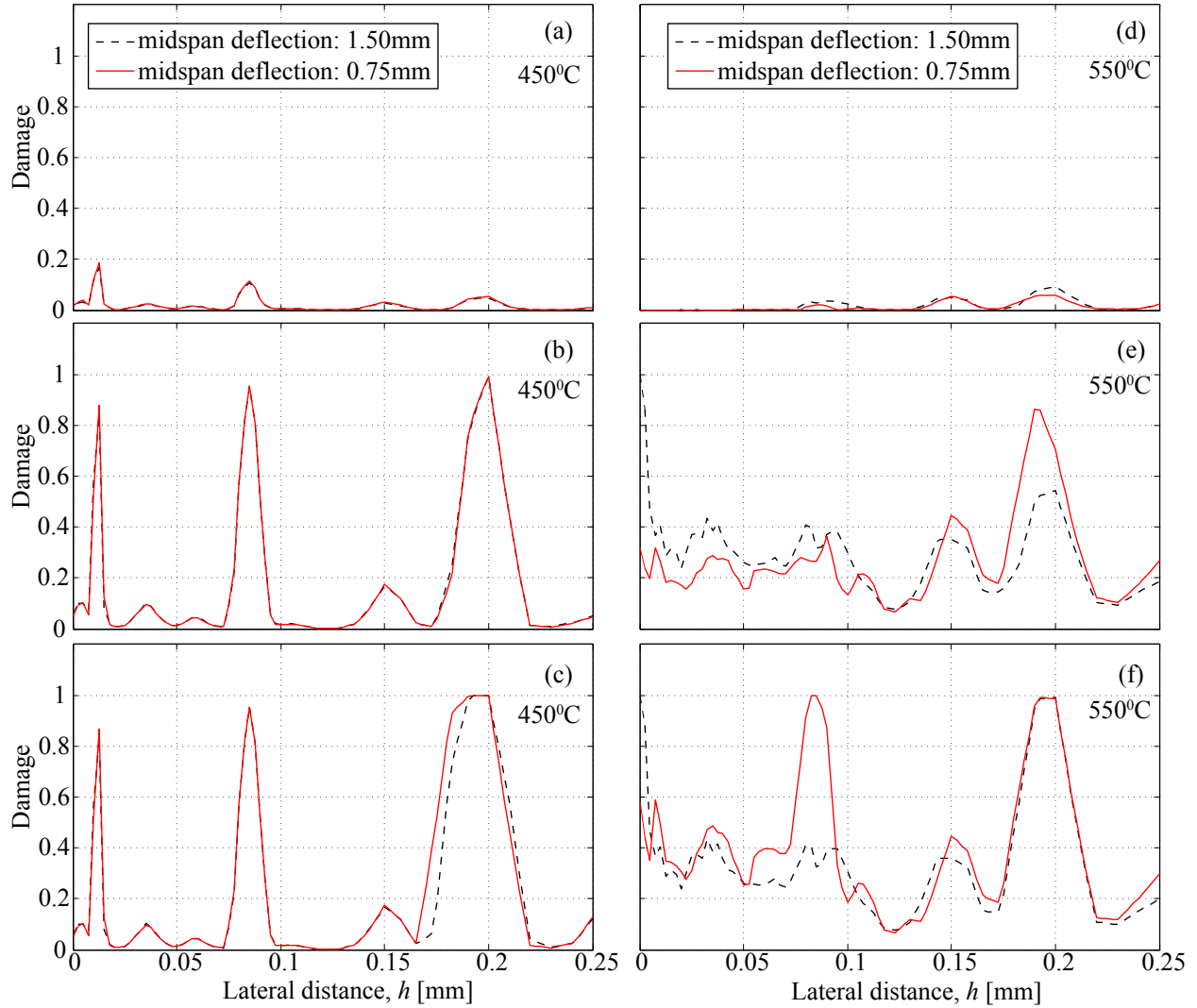


Figure 17: 3 point bending damage profile of the specimen oxidized at  $450^{\circ}\text{C}$  along tensile surface at applied displacement of: (a) 1.4 mm; (b) 2.1 mm; (c) 3.7 mm; at  $550^{\circ}\text{C}$  along tensile surface at applied displacement of (d) 1.35 mm; (e) 1.875 mm; (f) 2.475 mm.

experimentally observed crack spacing of 22 cracks/mm and 9 cracks/mm, respectively as summarized in Table 3. The thickness of the brittle surface layer is increased with increasing temperature because of the higher diffusivity of oxygen at elevated temperatures. The relationship between the spacing between the periodic embrittlement-induced surface cracks and the thickness of the brittle surface layer was investigated by Hutchinson and Suo [11], Thouless et al. [34] and others. The saturation crack spacing is proportional to the crack length to the first order of approximation. This relationship is due to the increased fracture process zone around the longer surface cracks compared to the shorter cracks. Under a critical stress magnitude, cracks start to form on the brittle layer and the stresses at the ligament around the crack relax. With increase in loading, more cracks progressively form until the saturation is reached where the shear stress at the interface of the brittle case and the substrate reaches its maximum allowable [26].

## 5 Conclusion

This manuscript provided a viscoelastic-viscoplastic model to describe the mechanical response of titanium structures operating under high temperature and mechanical loading. The effects of temperature-activated oxygen ingress into the structure and consequent embrittlement and hardening are included by considering a fully coupled transport model to the proposed deformation model. A suite of experiments on a high temperature alloy, Ti-6242S, has been employed to calibrate the model parameters and to understand the coupled mechanisms of oxygen ingress induced embrittlement, viscous relaxation/creep and deformation.

The experimental and the numerical investigations suggest that directly quantifying the effect of stress or strain state on the oxygen ingress rate is not straightforward. In a displacement-controlled setup, viscoelastic relaxation quickly reduces the internal stress, and hence, the load effect on oxygen ingress. In contrast, the effect of small changes in the oxygen ingress rate due to loading may be significant for cyclic loading cases, where the interactions of loading and the oxygen ingress rate may have a cumulative effect on crack initiation. Despite such difficulties, the proposed model accurately captures the coupled deformation-relaxation-embrittlement response at high temperature environments.

The experimental data employed in this manuscript to calibrate and validate the relaxation behavior is not exhaustive. While, it is beyond the scope of this manuscript to perform a comprehensive suite of experiments to fully characterize and connect the proposed model to the microstructural origins of relaxation, the need to further testing on creep-relaxation regime including a detailed microstructure study is important to link the relaxation behavior to the material microstructure, which is quite complex for Ti-6242S. A more systematic experimental study could clarify the sources of relaxation, and point to the effect of microstructure evolution on creep and relaxation, which is not included in this study.

From the modeling perspective, further improvements to the proposed computational model are necessary to understand and predict the behavior of titanium alloys operating in high thermo-mechanical environments. First, the model will be extended to describe the cyclic behavior to accurately predict initiation of fatigue damage, which is significantly affected by oxygen ingress. It is also clear that the oxygen ingress is localized within a very small boundary region of the structure with a thickness of the order of a few grain diameters. Accurate characterization of localized deformation and failure within this zone necessitates very fine resolution along the exposed surfaces [23, 24]. Straightforward biased meshing with such a refined resolution within a realistic structural component is not computationally feasible. A multi resolution modeling approach is necessary to accurately capture both the local (i.e., around the boundaries) and global (i.e., throughout the structure) response. Future research will focus on the development of such a multi resolution modeling approach.

## 6 Acknowledgements

The authors gratefully acknowledge the financial and technical support from the Air Force Research Laboratory, Structural Sciences Center (Contract No: GS04T09DBC0017 through High Performance Technologies, Inc.) and the Air Force Office of Scientific Research Multi-Scale Structural Mechanics and Prognosis Program (Grant No: FA9550-13-1-0104. Program Manager: Dr. David Stargel).

## References

- [1] S. Arbabi and M. Sahimi. Mechanics of disordered solids. I. Percolation of elastic networks with central forces. *Phys. Rev. B*, 47:695–702, 1993.
- [2] T. B. Belytschko, W. K. Liu, B. Moran, and K. I. Elkhodary. *Nonlinear Finite Elements for Continua and Structures*. Wiley, 2014.
- [3] W. J. Boettinger, M. E. Williams, S. R. Coriell, U. R. Kattner, and B. A. Mueller. Alpha case thickness modeling in investment castings. *Metall. Mater. Trans. B*, 31B: 1419–1427, 2000.
- [4] J. L. Chaboche. Thermodynamic formulation of constitutive equations and application to the viscoplasticity and viscoelasticity of metals and polymers. *Int. J. Solids Struct.*, 34:2239–2254, 1997.
- [5] K. S. Chan, M. Koike, B. W. Johnson, and T. Okabe. Modeling of alpha-case formation and its effects on the mechanical properties of titanium alloy castings. *Metall. Mater. Trans. A*, 39:171–180, 2008.

- [6] M. J. Donachie. *Titanium: A Technical Guide*. ASM International, 2nd edition, 2000.
- [7] J. Fish and C. Oskay. A nonlocal multiscale fatigue model. *Mech. Adv. Materials and Structures*, 12:485–500, 2005.
- [8] L. P. Franca, S. L. Frey, and T. J. R. Hughes. Stabilized finite element methods: I. Application to the advective-diffusive model. *Comp. Methods Appl. Mech. Engrg.*, 95:253–276, 1992.
- [9] L. P. Franca, H. Guillermo, and A. Masud. Revisiting stabilized finite element methods for the advective–diffusive equation. *Comput. Methods Appl. Mech. Engrg.*, 195:1560–1572, 2006.
- [10] R. M. Hinterhoelzl and R. A. Schapery. FEM implementation of a three-dimensional viscoelastic constitutive model for particulate composites with damage growth. *Mechanics of Time-Dependent Materials*, 8:65–94, 2004.
- [11] J. Hutchinson and Z. Suo. Mixed mode cracking in layered materials. *Adv. Appl. Mech.*, 29:63–191, 1992.
- [12] R. G. Keanini, G. K. Watkins, T. Okabe, and M. Koike. Theoretical study of alpha case formation during titanium casting. *Metall. Mater. Trans. B*, 38:729–732, 2007.
- [13] S. Kirkpatrick. Percolation and conduction. *Rev. Mod. Phys.*, 45:574–588, 1973.
- [14] D. Krajcinovic, M. Basista, K. Mallick, and D. Sumarac. Chemo-micromechanics of brittle solids. *J. Mech. Phys. Solids*, 40:965–990, 1992.
- [15] H. P. Langtangen. *Computational Partial Differential Equations: Numerical Methods and Diffpack Programming*. Springer, 2003.
- [16] C. Leyens and M. Peters. *Titanium and Titanium Alloys*. Wiley-VCH, 2003.
- [17] C. Leyens, M. Peters, D. Weinem, and W. A. Kaysser. Influence of long-term annealing on tensile properties and fracture of near- $\alpha$  titanium alloy ti-6al-2.75sn-4zr-0.4mo-0.45si. *Metall. Mater. Trans. A*, 27A:1709–1717, 1996.
- [18] J. C. M Li, R. A. Oriani, and L. S. Darken. Thermodynamics of stressed solids. *Zeitschrift Fur Physikalische Chemie-Frankfurt*, 49(3-5):271, 1966.
- [19] Z. Liu and G. Welsch. Literature survey on diffusivities of oxygen, aluminum and vanadium in alpha titanium, beta titanium, and in rutile. *Metall. Trans. A*, 19:1121–1125, 1988.

- [20] C. D. Lorenz, R. May, and R. M. Ziff. Similarity of percolation thresholds on the HCP and FCC lattices. *J. Stat. Phys.*, 98:961–970, 2000.
- [21] C. McAuliffe and H. Waisman. Mesh insensitive formulation for initiation and growth of shear bands using mixed finite elements. *Comp. Mech.*, 51:807–823, 2013.
- [22] K. S. McReynolds. A study on alpha case depth in Ti-6Al-2Sn-4Zr-2Mo. Technical Report AFRL-RX-WP-TP-2011-4294, Air Force Research Laboratory, 2011.
- [23] C. Oskay. Variational multiscale enrichment for modeling coupled mechano-diffusion problems. *Int. J. Numer. Meth. Engng.*, 89:686–705, 2012.
- [24] C. Oskay. Variational multiscale enrichment method with mixed boundary conditions for modeling diffusion and deformation problems. *Comput. Methods Appl. Mech. Engrg.*, 264:178–190, 2013.
- [25] C. Oskay and M. Haney. Computational modeling of titanium structures subjected to thermo-chemo-mechanical environment. *Int. J. Solids Struct.*, 47:3341–3351, 2010.
- [26] T. A. Parthasarathy, W. J. Porter, S. Boone, R. John, and P. Martin. Life prediction under tension of titanium alloys that develop an oxygenated brittle case during use. *Scripta Materialia*, 65(5):420–423, 2011.
- [27] P. W. M. Peters, J. Hemptenmacher, and C. Todd. Oxidation and stress enhanced oxidation of Ti-6-2-4-2. In *Ti-2003 Science and Technology. Proceedings of the 10th World Conference on Titanium*, 2003.
- [28] A. L. Pilchak, W. J. Porter, and R. John. Room temperature fracture processes of a near- $\alpha$  titanium alloy following elevated temperature exposure. *J. Mater. Sci.*, 47:7235–7253, 2102.
- [29] A. L. Ruoff and R. W. Balluffi. On strain enhanced diffusion in metals. iii. Interpretation of recent experiments. *J. Appl. Phys.*, 34:2862–2872, 1963.
- [30] R. L. Salganik. Transport processes in bodies with a large number of cracks. *Journal of Engineering Physics and Thermophysics*, 27(1534-1538), 1974.
- [31] J. L. Shannon Jr. Ti-6242. In *Aerospace Structural Metals Handbook*. 1978.
- [32] R. N. Shenoy, J. Unnam, and R. K. Clark. Oxidation and embrittlement of ti-6al-2sn-4zr-2mo alloy. *Oxidation of Metals*, 26:105–123, 1986.
- [33] K. V. S. Srinadh and V. Singh. Oxidation behaviour of the near  $\alpha$ -titanium alloy IMI 834. *Bull. Mater. Sci.*, 27:347–354, 2004.

- [34] M. D. Thouless, E. Olsson, and A. Gupta. Cracking of brittle films on elastic substrates. *Acta Materialia*, 40:1287–1292, 1992.
- [35] S. Yamanaka, H. Ogawa, and M. Miyake. Effect of interstitial oxygen on hydrogen solubility in titanium, zirconium and hafnium. *J. Less-Common Metals*, 172-174:85–94, 1991.
- [36] H. Yan and C. Oskay. A three field (displacement-pressure-concentration) formulation for coupled transport deformation problems. *Finite Elem. Anal. Des.*, 90:20–30, 2014.
- [37] H. W. Zhang, L. Sanavia, and B. A. Shreffler. An internal length scale in dynamic strain localization of multiphase porous media. *Mech. Cohes.-Frict. Mat.*, 4:443–460, 1999.